

Enhancement of H I absorption associated with the $z = 3.1$ large-scale proto-cluster and characteristic structures with AGNs sculptured over Gpc scale in the SSA22 field

T. Hayashino^{1*}, A. K. Inoue^{2,3}, K. Kousai¹, N. Kashikawa^{4,5,6}, K. Mawatari^{2,7}, Y. Matsuda^{4,5}, N. Tejos^{8,3}, J. X. Prochaska^{3,9}, I. Iwata^{5,10,11}, S. Noll^{12,13,14}, D. Burgarella¹⁵, T. Yamada^{16,17}, M. Akiyama¹⁶

¹Research Center for Neutrino Science, Graduate School of Science, Tohoku University, Aramaki, Aoba-ku, Sendai 980-8578, Japan

²Department of Environmental Science, Faculty of Design Technology, Osaka Sangyo University, 3-1-1, Nakagaito, Daito, Osaka 574-8530, Japan

³Department of Astronomy and Astrophysics, University of California Santa Cruz, 1156 High Street, Santa Cruz, CA 95064, USA

⁴National Astronomical Observatory of Japan, 2-21-1, Osawa, Mitaka, Tokyo 181-8588, Japan

⁵The Graduate University for Advanced Studies (SOKENDAI), Tokyo 181-8588

⁶Department of Astronomy, Graduate School of Science, The University of Tokyo, 7-3-1 Hongo, Bunkyo, Tokyo 113-0033, Japan

⁷Institute for Cosmic Ray Research, The University of Tokyo, 5-1-5 Kashiwanoha, Kashiwa, Chiba 277-8582, Japan

⁸Instituto de Física, Pontificia Universidad Católica de Valparaíso, Casilla 4059, Valparaíso, Chile

⁹University of California Observatories, Lick Observatory 1156 High Street, Santa Cruz, CA 95064, USA

¹⁰Subaru Telescope, National Astronomical Observatory of Japan, 650 North A'ohoku Place Hilo, HI 96720, USA

¹¹Department of Astronomy and Physics and Institute for Computational Astrophysics, Saint Mary's University, 923 Robie Street, Halifax, Nova Scotia B3H 3C3, Canada

¹²Institut für Astro- und Teilchenphysik, Universität Innsbruck, Technikerstr. 25/8, 6020 Innsbruck, Austria

¹³Institut für Physik, Universität Augsburg, Universitätsstr. 1, 86159 Augsburg, Germany

¹⁴Deutsches Fernerkundungsdatenzentrum, Deutsches Zentrum für Luft- und Raumfahrt, Münchener Str. 20, 82234 Weßling-Oberpfaffenhofen, Germany

¹⁵Laboratoire d'Astrophysique de Marseille, Observatoire Astronomique de Marseille-Provence, 38 rue Frédéric Joliot-Curie, 13388 Marseille Cedex 13, France

¹⁶Astronomical Institute, Graduate School of Science, Tohoku University, Aramaki, Aoba-ku, Sendai 980-8578, Japan

¹⁷Institute of Space and Astronautical Science, Japan Aerospace Exploration Agency, Kanagawa 252-5210, Japan

ABSTRACT

In the SSA22 field which exhibits a large-scale proto-cluster at $z = 3.1$, we carried out a spectroscopic survey for Lyman Break Galaxies (LBGs) with the VLT/VIMOS and identified 78 confident LBGs at $z = 2.5\text{--}4$. We stacked their spectra in the observer's frame by using a sophisticated method. Analyzing the composite spectrum, we have revealed that the large-scale proto-cluster at $z = 3.1$ has a strong H I absorption dip of rest-frame equivalent width of -1.7 \AA . Another strong absorption dip found at $z = 3.28$ is associated with a modestly high-density LBG peak, similar to that at $z = 3.1$. We have also detected an H I transparency peak at $z = 2.98$ in the composite spectrum, coincident with a void in the LBG distribution. In this paper, we also investigated the relation between LBGs, H I gas and AGNs at $z = 3\text{--}4$ in the SSA22 field. Two AGNs at $z = 3.353$ and 3.801 are, respectively, associated with the LBG concentration of an overdensity factor $\delta_{\text{LBG}} \simeq 2$ in the present statistics. Another structure at $z = 3.453$ is remarkable: 20 comoving Mpc scale dense H I gas which is not associated with any apparent LBG overdensity but involving a pair of AGNs. Such structure may be a new type of the AGN-matter correlation. If the inhomogeneous structures over a comoving Gpc scale found in this paper are confirmed with sufficient statistics in the future, the SSA22 field will become a key region to test the standard cold dark matter structure formation scenario.

Key words: cosmology: observations — large-scale structure of Universe — galaxies: active — galaxies: high-redshift — intergalactic medium

1 INTRODUCTION

Regions showing galaxy concentration at high redshift are important places to study formation and evolution of galaxies as well as cosmological structures. Among them, the proto-cluster (PC) at $z = 3.1$ in the SSA22 field, initially discovered by Steidel et al. (1998) can be called “a treasure island” of the Universe. In 1998, they found out a number density peak of Lyman Break Galaxies (LBGs) with the overdensity of $\delta \sim 5$ at $z = 3.1$, and their narrow-band (NB) imaging survey for the peak in 2000 detected 72 Ly α emitters (LAEs) as well as two gigantic Ly α emitting objects so-called Ly α blobs (LABs) together with about a dozen of Ly α absorbers (LAAs) in their $9' \times 9'$ survey field, SSA22a (Steidel et al. 2000).

Following this, a deep NB imaging survey was carried out in 2002 in a field centered on the PC, SSA22a with Subaru Suprime-Cam (S-Cam) having a wide field of view (FoV) of $35' \times 27'$ to see the environment of the PC (Hayashino et al. 2004). We call the survey area SSA22 Sb1 or simply Sb1 in this paper. As a result, 283 highly confident LAEs exhibiting a belt-like large-scale structure were found, i.e., it is revealed that the PC by Steidel et al. is not isolated in high-redshift space, but a part of the much larger structure. Interestingly, “the belt” extends to the edge of the field of view, being 60 or more comoving Mpc long. In this survey, around 30 LABs (Matsuda et al. 2004) and LAAs (Hayashino et al. 2004) are found in the belt-like structure besides LAEs and LBGs. Here LABs are expected to be a progenitor of massive galaxies in the present Universe (e.g., Uchimoto et al. 2012). Thus, the belt-like large-scale structure found in the Sb1 field is like a factory producing various kinds of galaxies in the young Universe and can be called the “large-scale proto-cluster (LSPC)”. “The belt” would evolve to a filament of the present-day large-scale structure and the PC discovered by Steidel et al. would collapse to a massive cluster of galaxies at present (e.g., Topping et al. 2018). Objects in the structure of Sb1 characterized by Ly α emission or absorption have also been investigated so far in various wavelengths from sub-mm to X-ray.

In succession, a panoramic NB imaging survey was performed to reveal the entire extent of the structure seen in Sb1 as an Intensive Program of Subaru telescope in 2005 (Yamada et al. 2012a). The area of 7 S-Cam FoVs around the SSA22-Sb1 was observed in the panoramic survey of 200 Mpc \times 100 Mpc in comoving scale. In the survey, around 1400 LAEs and 100 LABs were detected. This survey reveals farther lateral extension of the LSPC. A wide sky map of the LAEs is displayed in Yamada et al. (2012a). By the stacking analysis of Ly α images in high statistics from the panoramic survey, Matsuda et al. (2012) have found that LAEs have large Ly α emitting halos extended to 60 proper kpc showing an interesting dependence, i.e., larger halos for higher LAE local density in Mpc scales. The correlation between the Ly α halo size of individual objects and their Mpc scale environment is indeed remarkable, implying interactions of these galaxies with neutral hydrogen atoms in that scale probably controlled by the dark matter gravitation, and suggesting the importance of studies on H I gas in the LSPC. Also, by stacking Ly α images of LBGs in their large sample, Steidel et al. (2011) confirmed extended Ly α halos

around LBGs, which had been first detected in naive form in the SSA22 PC at $z = 3.1$ by Hayashino et al. (2004).

In the panoramic survey area of the 200 Mpc \times 100 Mpc comoving scale, the PC found by Steidel et al. (1998) in Sb1 is still the highest density peak and two LABs discovered by them are the biggest two of all LABs found in the panoramic field. So, the Sb1 field including the original PC would be the most important region to be intensively studied. Indeed, successive spectroscopic observations of LBGs, LAEs and LABs in Sb1 have been performed (Matsuda et al. 2005, 2006; Kousai 2011; Yamada et al. 2012b; Saez et al. 2015; Topping, Shapley & Steidel 2016) and the three-dimensional structure of “the belt” and the PC have been discussed (Matsuda et al. 2005; Kousai 2011; Topping et al. 2018).

It is fundamentally important to measure H I abundance of such structure to understand galaxy formation in a PC with high galaxy density, because many kinds of objects in the structure characterized by strong Ly α emission and/or absorption form and evolve by using neutral hydrogen that may be supplied from the structure. From this viewpoint, a dense H I region associated with a high LBG density peak at $z = 2.895$ recently discovered by Cucciati et al. (2014) in the COSMOS field in the VIMOS Ultra-Deep Survey (VUDS) is noteworthy. While Cucciati et al. (2014) only probed H I at the PC redshift, the Wiener-filtered tomographic survey in the COSMOS field by Lee et al. (2014a,b, 2016, 2018) presents interesting and impressive results on the correlation of the three-dimensional LBG distribution and H I absorption map on comoving Mpc scales in a wide redshift range of $2.0 < z < 2.6$.

In 2008, we performed yet another spectroscopic survey with VLT/VIMOS, hereafter VI08, having a wide field of view, to reveal LBG distribution in foreground and background of the $z = 3.1$ LSPC. Namely, we tried a longitudinal, i.e., line-of-sight, extension of the survey region from the narrow redshift range of $z = 3.06$ – 3.12 sliced by the NB filter for LAEs to a wider redshift range around $z = 3$ selected by the U-dropout method for LBGs. As we will see in this paper, the VI08 survey has revealed 30 or more LBGs behind the LSPC at $z = 3.1$. These LBGs should have important information on H I of the LSPC in their spectra. Here, LBGs are not as bright as QSO/AGNs but they have a higher comoving density. So, the individual LBG spectrum may be noisy to obtain significant information on LSPC H I. However, if we stack these spectra in the observer’s frame to improve a signal to noise ratio (S/N), information on H I gas in the LSPC imprinted will appear. Also, the stacked spectrum would reveal H I gas distribution in foreground and background of the LSPC, which we present in this paper.

As a companion analysis, we have also tried to map the H I absorption distribution at the PC redshift $z = 3.1$ by using our deep NB imaging data with higher S/N than the individual spectra of the VI08 survey, which is reported in Mawatari et al. (2017). In the NB photometric data of galaxies behind the $z = 3.1$ PC, information on H I absorption is imprinted in the spectra. This method is especially very effective to study absorption with the similar wavelength widths as the NB filter and to depict the two-dimensional map of H I gas. Interestingly, an H I absorption excess is observed throughout the Sb1 area corresponding to a size larger than 50 comoving Mpc (Mawatari et al. 2017).

Also, in the SSA22 field, Sb1, around 10 AGNs are already detected at redshifts between $z = 3$ and 4 in the precedent studies (Lehmer et al. 2009; Saez et al. 2015; Micheva, Iwata, & Inoue 2017). Therefore, we are able to investigate H I and LBG distributions as well as their connection with the AGNs in these redshifts, which is another theme presented in this paper.

The following is the structure of this paper; in the next section, we describe the imaging and spectroscopic data of LBGs in the SSA22-Sb1 field. In section 3, we present the method of the observer’s frame composite to examine H I with high S/N. In section 4, we show the results obtained from the observer’s frame composite analysis and investigate a correlation between the LBG distribution and H I absorption. In section 5, we consider the over-density mass and the appearance probability of the LSPC at $z = 3.1$ as well as characteristic surroundings showing H I transparency. In section 6, we discuss inhomogeneous distributions of LBGs associated with AGNs at $z = 3-4$ and present a dense H I region involving a pair AGN. The final section is devoted to our conclusions. In appendix, we present a catalog of the VI08 LBGs. We assume the flat Universe with cosmological parameters of $H_0 = 70 \text{ km s}^{-1} \text{ Mpc}^{-1}$, $\Omega_m = 0.3$, and $\Omega_\Lambda = 0.7$. The magnitude unit throughout this paper is the AB system.

2 SAMPLE OF LYMAN BREAK GALAXIES

2.1 Photometric data and color selection

The photometric data we used are B , V , R_c , i' , and z' -band imaging taken with Subaru/S-Cam (Miyazaki et al. 2002) and u^* band imaging taken with Canada-France-Hawaii Telescope (CFHT)/Megacam (Boulade et al. 2003). The observations and data reduction for the S-Cam data are described in Hayashino et al. (2004). The Megacam data was downloaded from the CFHT archive and reduced by a standard manner described in Kousai (2011) and references therein. The $1-\sigma$ limiting magnitudes in each band are 27.8 (u^*), 28.2 (B), 28.2 (V), 28.3 (R_c), 27.9 (i'), and 27.2 (z') for a $2''$ diameter aperture. We selected LBGs from objects detected in R_c by the following color selection criteria similar to those adopted in literature (e.g., Steidel et al. 1995; Yoshida et al. 2008):

- (i) $23.9 \leq R_c \leq 25.4$
- (ii) $(U - V) - 1.8(V - R_c) \geq 1.1$
- (iii) $R_c - i' \leq 0.3$

The faint magnitude limit of the criterion (i) is determined to select LBGs bright enough to detect their continuum in the follow-up spectroscopy.

2.2 Spectroscopic data and redshift determination

We performed spectroscopy for the selected LBGs with Visible Multi-Object Spectrograph (VIMOS; Le Fèvre et al. 2003) on Very Large Telescope (VLT) under the program ID of 081.A-0081(A) (PI: A. K. Inoue). We used the LR-Blue/OS-Blue setting where the spectral resolving power $R = \lambda/\Delta\lambda \simeq 180$ and the pixel scale is $5.3 \text{ \AA}/\text{pix}$. With VIMOS, we can observe 4 quadrants with about 2 arcmin

separation simultaneously in one pointing, for a total FoV of about $14 \times 16 \text{ arcmin}^2$ in each pointing. We observed 2 pointings whose coordinates, observed month, exposure time, and seeing are listed in Table 1. We had 623 LBGs satisfying the selection criteria described above in the two FoVs, out of which we observed 163 objects. We avoided galaxies which had spectroscopic redshifts previously obtained. This would cause a bias in the galaxy selection, but we did not correct it in the expected redshift distribution described in the next subsection.

The data reduction was done with the VIMOS pipeline recipes¹ and the NOAO/IRAF². We used the pipeline software only to make bias and flat frames. Other steps were done with IRAF through the standard manner (see Kousai 2011 in detail). During the data reduction, we found that the data quality in a quadrant of FoV-1 was very low because there was no object in a half of the images obtained from this quadrant. This might be caused by a displacement of the slit mask for the quadrant in observations. We decided to discard this quadrant unfortunately.

To produce the one-dimensional spectrum of each LBG, we extracted spatially 4 pixels tracing the object continuum from the background subtracted and median coadded two-dimensional spectral image, and summed them up. Given the spatial pixel scale of $0.205''/\text{pix}$, the extracted spatial scale is 0.82 arcsec which was chosen to maximize the S/N ratio for the continuum rather than to collect the total flux of the objects.

We have determined Ly α emission/absorption and metal absorption redshifts ($z_{\text{Ly}\alpha}$ and z_{metal}) of the LBGs by eye after applying a 5-pix box-car smoothing to the one-dimensional spectra. The 5-pix almost corresponds to the spectral resolution of the VIMOS LR-Blue setting with $R = 180$ and $5.3 \text{ \AA}/\text{pix}$. The spectral features which we searched for were Ly α emission/absorption (1215.67 \AA in the source rest-frame), Ly β (1025.72 \AA) and Ly γ (972.54 \AA) absorption lines, Si II (1260.42 \AA), O I (1302.17 \AA), Si II (1304.37 \AA), C II (1334.53 \AA), Si IV (1393.76 and 1402.77 \AA), Si II (1526.71 \AA), C IV (1548.20 and 1550.78 \AA), Fe II (1608.45 \AA), and Al II (1670.79 \AA) absorption lines, and He II (1640.4 \AA) emission. We also searched [O II] (3727.5 \AA), H β (4861.3 \AA), [O III] (4958.9 and 5006.8 \AA), and H α (6562.8 \AA) emission lines as a signature of low redshift contamination.

We have classified the redshifts into four categories: Ae (clear Ly α emission is identified), Aa (clear Ly α absorption and several clear metal absorption lines are identified), B (Ly α absorption and a few metal absorption lines are identified), and C (possible Ly α emission/absorption and/or possible metal absorption are identified). Figure 1 shows example spectra of the four categories. The resultant numbers of $z \sim 3$ LBGs are summarized in Table 2.

According to Adelberger et al. (2005), the redshift of the Ly α emission line is slightly redshifted compared to those of the nebular emission lines in the rest-frame optical which are more reliable as the systemic redshifts. On the other hand, the redshifts of the metal absorption lines are slightly blueshifted compared to those of the optical nebular lines. Then, we adopt the calibration formulae proposed by

¹ <http://www.eso.org/sci/software/pipelines/vimos/>

² <http://iraf.noao.edu/>

Table 1. Summary of VIMOS observations for the SSA22 field.

	RA (J2000)	DEC (J2000)	Observations	Exposure time (s)	Seeing (arcsec)	Remark
FoV-1	22:17:31.9	+00:24:29.7	July–October 2008	14,080	0.32–1.93	Loss of quadrant #2
FoV-2	22:17:39.1	+00:11:00.7	August–October 2008	14,080	0.48–1.37	

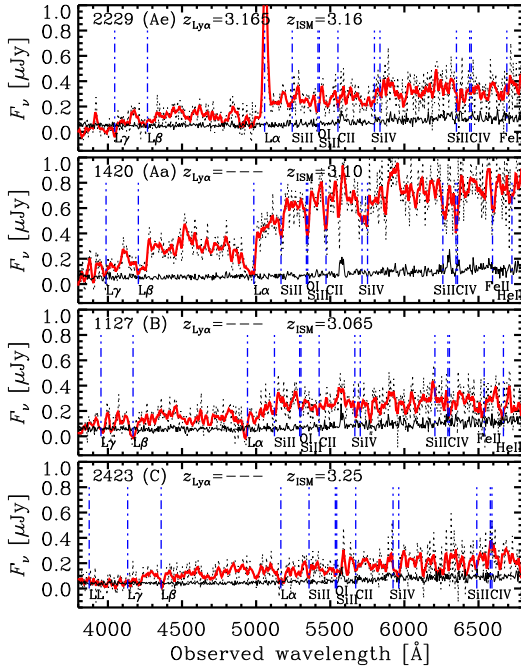


Figure 1. Example one-dimensional spectra of the four redshift categories. The thick solid and thin dotted lines are the object spectra with and without a 5-pix box-car smoothing, respectively. The thin solid lines are the root-mean-square spectra of the sky-subtracted background. The vertical dot-dashed lines show the wavelengths of some emission/absorption lines and the Lyman limit (LL). (a) Ae: clear Ly α emission is identified, (b) Aa: clear Ly α absorption and several clear metal absorption lines are identified, (c) B: Ly α absorption and a few metal absorption lines are identified, and (d) C: possible Ly α emission/absorption and/or possible metal absorption are identified.

Adelberger et al. (2005) to estimate the systemic redshifts of the LBGs. For LBGs with the Ly α emission line, we adopt

$$z_{\text{sys}} = z_{\text{Ly}\alpha} - 0.0033 - 0.0050(z_{\text{Ly}\alpha} - 2.7), \quad (1)$$

and for LBGs without the Ly α emission line, we adopt

$$z_{\text{sys}} = z_{\text{metal}} + 0.0022 + 0.0015(z_{\text{metal}} - 2.7). \quad (2)$$

The uncertainties of $z_{\text{Ly}\alpha}$ and z_{metal} are ≈ 0.005 estimated from the wavelength pixel scale of $5.3 \text{ \AA}/\text{pix}$. The uncertainties of equations (1) and (2) are ≈ 0.003 (Adelberger et al. 2005). If we take the summation in quadrature, the uncertainty of z_{sys} is ≈ 0.006 . Although there are updates of these formulae, for example, by Steidel et al. (2010) and Turner et al. (2014), the accuracy of the redshifts in equations (1) and (2) is sufficient for our analysis because we make a composite in the observer’s rest-frame not in the galaxies’ rest-frame.

Table 2. Summary of VIMOS redshift survey results in the SSA22 field.

Area (arcmin ²)	322
N_{cand}^a	623
N_{spec}^b	163
N_{Ae}^c	39
N_{Aa}^c	18
N_{B}^c	21
N_{C}^c	21

^a Number of the photometric LBG candidates.

^b Number of the objects observed in the spectroscopy.

^c Number of the objects classified into each category.

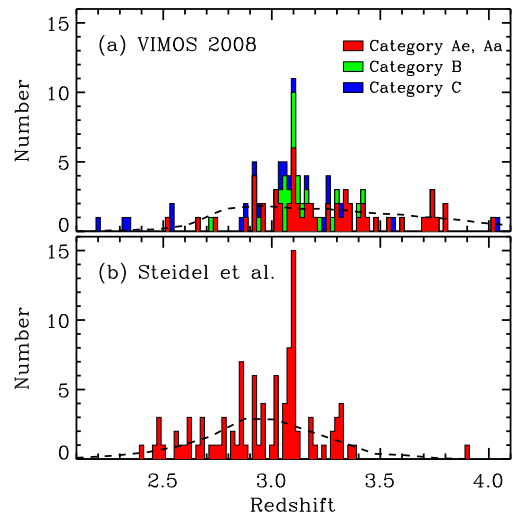


Figure 2. Spectroscopic redshift distributions of LBGs by (a) the VIMOS survey in 2008 and (b) Steidel et al. (2003). For the VIMOS survey, we show the different redshift categories (i.e., qualities) by different colors as indicated in the panel. The dashed lines are the expected distributions in each survey assuming a uniform distribution of galaxies.

2.3 Redshift distribution of the LBGs

The redshift distribution of the LBGs in our survey is shown in the top panel of Figure 2, while that of the survey of Steidel et al. (2003) in the same field is shown in the bottom panel of the figure. We find several redshift spikes in these distributions. In particular, the strongest peak is $z = 3.1$. This is the redshift of the huge overdensity of galaxies previously known in this field (Steidel et al. 1998, 2000; Hayashino et al. 2004; Matsuda et al. 2004, 2005; Yamada et al. 2012a; Saez et al. 2015; Topping et al. 2018).

In the top panel, we also show the expected number distribution from our photometric selection criteria if the galaxies were distributed uniformly in the Universe. The ex-

pected number of galaxies at the redshift between z and $z + \Delta z$ is given by

$$N_{\text{exp}}(z) = \int_{M_{\text{min}}}^{M_{\text{max}}} \phi(M) \int_z^{z+\Delta z} C(z', M) \frac{dV}{dz}(z') dz' dM, \quad (3)$$

where $\phi(M)$ is the number density of LBGs with the absolute magnitude M (i.e., luminosity function), $C(z, M)$ is the selection efficiency for an object with M at z (i.e., completeness), and $dV/dz(z)$ is the volume element. We assume the luminosity function of $z \sim 3$ LBGs reported by Steidel et al. (1999) for $\phi(M)$. The integration boundaries are set to be $M_{\text{min}} = -24.0$ and $M_{\text{max}} = -17.0$ which do not affect the result very much because the magnitude limit described in section 2.1 is included in $C(z, M)$.

To obtain $C(z, M)$, we have performed a Monte-Carlo simulation of our color selection. First, we generated a large number of mock galaxies having z , M , and a spectrum. For the spectrum, we prepared 4 types depending on the Ly α strength as reported by Steidel et al. (2003). These four spectra were produced based on the population synthesis model GALAXEV (Bruzual & Charlot 2003) to extend shorter and longer wavelengths than those observed by Steidel et al. (2003). We then applied a mean IGM transmission by Inoue et al. (2005). Second, we calculated apparent magnitudes from u^* to z' of the mock galaxies based on their spectra, redshift z , and M . Then, we randomly added Gaussian errors based on the limiting magnitude in each band to the apparent magnitudes. In this step, we mixed the 4 types of spectra with an equal weight. Finally, we applied the color (and magnitude) selection to them and counted the number fraction selected as a function of (z, M) .

Since we did not observe all galaxies satisfying the color selection and could measure redshifts for only a part of the observed galaxies, we cannot compare the expected number of galaxies in equation (3) with the obtained redshift distribution directly. Therefore, we normalized the expected number distribution by the total number of galaxies for which we measured their redshifts successfully, following Steidel et al. (1998, 2000, 2003).

The expected distribution in Steidel et al.'s survey in the bottom panel of Figure 2 is empirically obtained from the sum of 17 different fields of their spectroscopic survey. The distribution is again normalized by the total number of the redshifts in the SSA22 field. The shape of their empirical distribution function of LBGs is quite different from our expected one. This is because they used a different filter set and applied a different color selection from those we did.

3 OBSERVER'S FRAME COMPOSITE SPECTRUM

Using the VIMOS LBG spectra, we examine the IGM H I fluctuation along the sight-line of the SSA22 field. The continuum S/N ratio per wavelength element in the so-called "DA" (Depression at Ly α) wavelength range of the individual LBG spectra distributes from 1 to 8 and the median is about 3. Thus, we adopt a stacking technique to increase the S/N ratio. Since we are investigating the IGM, we make an observer's frame composite spectrum. This composite analysis also means that we will examine an average of the H I

fluctuation over the observing field. In this analysis, we restrict ourselves to the spectra categorized as Ae, Aa, and B to avoid possible contamination of lower- z spectra in the category C. In addition, we remove one object in the category Ae (Slit #2408) because of its low S/N in the continuum (S/N ~ 0.2 in the DA range). Therefore, we use 77 LBG spectra in total.

Here, we propose a new method to make an observer's frame composite rather than a simple sum of the spectra over the whole wavelength coverage as done by Cucciati et al. (2014) in order to avoid contamination of galaxies' Ly α emission/absorption line and many interstellar absorption lines in the resultant composite spectrum. The intergalactic Ly β absorption lines also contaminate the spectrum for the highest redshift LBGs. In order to isolate the intergalactic H I Ly α absorption, we stack only the wavelength range between Ly α and Ly β in the source rest-frame, the so-called DA range. There is a small contamination of narrow absorption lines by other atoms like C, O, and so on in the IGM at lower redshift. We neglect it because we can not identify these lines in our low-resolution and low S/N ratio spectra. However, this effect has been estimated to be as small as 3% in terms of the transmission at $z = 3$ (Faucher-Giguère et al. 2008). On the other hand, some metal absorption lines in the stellar photosphere and in the ISM of galaxies may contaminate in the spectral range. In the rest-frame composite spectra of $z \sim 2-3$ galaxies reported by Shapley et al. (2003) and Steidel et al. (2010), we can identify Si IV $\lambda 1063$, N II $\lambda 1084$, and C III $\lambda 1178$ lines between Ly α and Ly β . Then, we define the DA range as 1070–1170 Å with a narrow mask of 6.5 Å (= 5 pix at $z \sim 3$) around 1084 Å in the source rest-frame to avoid these metal lines as well as any effects of broad Ly α and Ly β absorption features of the emitting galaxy itself. The final wavelength width to be used in the composite is about 370 Å in the observer's frame and about 70 pixels, corresponding to $\Delta z \approx 0.3$ for H I Ly α .

3.1 Procedure to make the DA range composite spectrum

The procedure for making the observer's frame composite spectrum consists of the following 3 steps:

- (i) Clip out the DA range in the source rest-frame from each one-dimensional observed spectrum without any smoothing: $f_{\nu_{\text{DA}}}^{\text{obs}}$.
- (ii) Make a linear fit of the clipped-out spectrum³ and normalize it by the fit: $\tilde{f}_{\nu_{\text{DA}}} = f_{\nu_{\text{DA}}}^{\text{obs}} / f_{\nu_{\text{DA}}}^{\text{fit}}$.
- (iii) Make a median or 3- σ clipping average composite of the normalized spectra in the observer's frame.

³ We used all the wavelength pixels in the DA range, except for several pixels possibly affected by N II $\lambda 1084$ absorption, for this linear fit because the possible IGM H I absorption enhancement would be narrow enough relative to the entire DA range and would not affect the fit very much. Indeed, we have confirmed that the $z = 3.1$ H I enhancement is robust even if we applied $N\sigma$ -clipping to the linear fitting. For $N = 0.5, 1, 2, \text{ or } 3$, we have found -35% , $+16\%$, -7% , or -3% change in the *excess* equivalent width, respectively, which are comparable or smaller than the uncertainty obtained by a bootstrap method.

After making the composites, we apply a 5-pix boxcar smoothing to the spectra. The choice of 5 pixels is based on the spectral resolution of our VIMOS observations with LR-Blue/OS-Blue ($R \simeq 180$ and pixel scale of $5.3 \text{ \AA}/\text{pix}$). The 5 pixels also correspond to a scale of about 20 comoving Mpc at $z = 3.1$ for H I Ly α . This scale is very similar to the transverse scale of the filaments in the overdensity structure traced by LAEs at $z = 3.1$ (Hayashino et al. 2004; Yamada et al. 2012a). Therefore, we can examine a structure larger than this scale along the sight-line in the composite spectrum.

The physical meaning of the normalized spectrum, \tilde{f}_ν , is the fluctuation of the H I absorption relative to an average one as we find from the following discussion. If we express the IGM H I Ly α optical depth along a sight-line as

$$\tau_{\nu(z)}^{\text{IGM}} = \langle \tau_{\nu(z)}^{\text{IGM}} \rangle + \delta\tau_{\nu(z)}^{\text{IGM}}, \quad (4)$$

where $\langle \tau_{\nu(z)}^{\text{IGM}} \rangle$ is the cosmic mean optical depth at the redshift z and $\delta\tau_{\nu(z)}^{\text{IGM}}$ is the fluctuation relative to the mean, the observed flux becomes

$$f_\nu^{\text{obs}} = e^{-(\tau_{\nu(z)}^{\text{IGM}})} e^{-\delta\tau_{\nu(z)}^{\text{IGM}}} f_\nu^{\text{cont}} = \langle T_\nu^{\text{IGM}} \rangle e^{-\delta\tau_{\nu(z)}^{\text{IGM}}} f_\nu^{\text{cont}}, \quad (5)$$

where f_ν^{cont} is the continuum before the IGM absorption, and $\langle T_\nu^{\text{IGM}} \rangle$ is the cosmic mean IGM transmission. If the period of the fluctuation $\delta\tau_{\nu(z)}^{\text{IGM}}$ is short enough relative to the DA range, the linear fit spectrum can be expressed as

$$f_\nu^{\text{fit}} = \langle T_\nu^{\text{IGM}} \rangle f_\nu^{\text{cont}}, \quad (6)$$

because the variation by $\delta\tau_{\nu(z)}^{\text{IGM}}$ is smoothed out. Therefore, we obtain

$$\tilde{f}_\nu = e^{-\delta\tau_{\nu(z)}^{\text{IGM}}}, \quad (7)$$

and

$$\delta\tau_{\nu(z)}^{\text{IGM}} = -\ln \tilde{f}_\nu \quad (8)$$

3.2 Composite of sky-subtracted background

The uncertainty caused by the fluctuation of the sky-subtracted background can be measured by making a composite of the sky-subtracted background spectra. We stack only the ‘‘DA range’’ of the sky-subtracted background based on each LBG’s redshift, as follows. First, in each sky-subtracted two-dimensional spectrum, we define 10 pixels along the spatial direction as the background region, avoiding pixels possibly including object flux. Then, we calculate the sum of the background brightness, $I_{\nu\text{DA}}^{\text{back}}$, of the 10 pixels for each wavelength element and scale it to the $N_{\text{pix}} = 4$ extraction so as to be equivalent to the object spectra. Namely, the sky-subtracted background spectrum $f_\nu^{\text{back}} = (N_{\text{pix}}/10)^{1/2} \sum_{i=1}^{10} I_{\nu}^{\text{back}}$. Next, we stack f_ν^{back} in the almost same way as the object spectra described in the previous subsection. However, f_ν^{back} distributes around zero because it is the residual of the sky subtraction. The linear fit and normalization in the step (ii) of the composite procedure causes erroneously large fluctuation. Thus, we replace the clipped-out spectrum of the step (i) with

$$f_{\nu\text{DA}}^{\text{obs}'} = f_{\nu\text{DA}}^{\text{fit}} + f_{\nu\text{DA}}^{\text{back}}. \quad (9)$$

The fit spectrum $f_{\nu\text{DA}}^{\text{fit}}$ is a linear fit of each object spectrum within the DA range: the same one used as the normalization in the step (ii) for the object composite. In the step (ii)

of this background composite, the replaced clipped-out spectrum is normalized by another linear fit function obtained from the replaced spectrum as:

$$\tilde{f}_{\nu\text{DA}} = f_{\nu\text{DA}}^{\text{obs}'} / f_{\nu\text{DA}}^{\text{fit}'}. \quad (10)$$

The last step in the procedure is the same. We also apply a 5-pix boxcar smoothing to the resultant composite.

3.3 Monte-Carlo simulation of the composite

To estimate the fluctuation of the composite spectrum caused by the Ly α forest (LAF) and observational errors (i.e., background fluctuation), we perform a Monte-Carlo simulation which generates a large number of mock observed spectra:

$$f_\nu^{\text{MC}} = T_\nu^{\text{IGM}} f_\nu^{\text{cont}} + \delta_\nu^{\text{back}}, \quad (11)$$

where ν is the frequency in the observer’s frame, T_ν^{IGM} is the intergalactic transmission, f_ν^{cont} is the continuum spectrum of galaxies, and δ_ν^{back} is the observational error caused by the sky-subtracted background fluctuation.

The intergalactic transmission T_ν^{IGM} is generated by the Monte-Carlo simulation model developed by Inoue & Iwata (2008). We adopt the latest version in which the statistics of IGM absorbers is updated (Inoue et al. 2014) although this update does not affect the transmission in the DA range significantly. In the simulation, we mimic our VIMOS observations as follows. The wavelength pixel scale of the observations is $5.3 \text{ \AA}/\text{pix}$. Since this resolution is too coarse to resolve fine absorption lines by the LAF, we adopt ten times finer resolution in the calculations: 0.53 \AA which corresponds to $\approx 0.1 \text{ \AA}$ in the rest-frame at $z = 3$. This resolution is fine enough to give a $\sim 1\%$ accuracy in transmission compared to that calculated with a 0.01 \AA resolution (Inoue & Iwata 2008). Then, we apply a smoothing with a Gaussian function whose FWHM is $\Delta\lambda = \lambda/R$, where the resolving power of $R = 180$ and a typical wavelength of $\lambda = 5000 \text{ \AA}$ in our observations. Finally, we average the resulting transmission values for intervals of 10 pixels to match the pixel scale of the VIMOS observations.

We note here that there is neither sight-line (i.e., redshift) nor spatial correlation of absorbers in our Monte-Carlo simulation. The absorbers follow their empirical distribution function but are completely randomly located from each other. However, the absorbers do correlate with themselves in the real Universe (e.g., Zuo & Bond 1994; Cristiani et al. 1995; Meiksin & Bouchet 1995; Croft et al. 1999; McDonald et al. 2000). Thus, our simulation underestimates the fluctuation of the IGM. On the other hand, we still have the sensitivity to detect the real IGM fluctuation with this random IGM simulation, examining if the resultant composite spectrum has fluctuation significantly larger than that expected from random.

The continuum f_ν^{cont} in the DA range is never observed because it is modulated by the LAF. Here we simply assume f_ν^{cont} to be constant in the DA range:

$$f_{\nu\text{DA}}^{\text{cont}} = \frac{\int_{\Delta\nu\text{DA}} f_\nu^{\text{obs}} / \langle T_\nu^{\text{IGM}} \rangle d\nu}{\Delta\nu\text{DA}}, \quad (12)$$

where f_ν^{obs} is the observed spectrum, $\langle T_\nu^{\text{IGM}} \rangle$ is a mean intergalactic transmission, and $\Delta\nu\text{DA}$ is the frequency interval

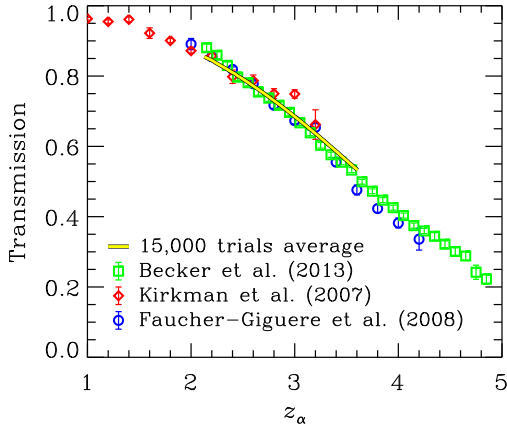


Figure 3. Intergalactic transmission as a function of the absorber’s redshift $z_\alpha = \lambda_{\text{obs}}/\lambda_\alpha - 1$, where λ_{obs} is the observed wavelength and $\lambda_\alpha = 1215.67 \text{ \AA}$ is the H I Ly α wavelength. The data points with error bars are taken from the literature as shown in the panel. The solid curve is the mean transmission obtained from our Monte-Carlo simulation described in equation (14).

of the DA range. The mean transmission is assumed to be

$$\langle T_\nu^{\text{IGM}} \rangle = e^{-\langle \tau_\nu^{\text{IGM}} \rangle}, \quad (13)$$

and

$$\langle \tau_\nu^{\text{IGM}} \rangle = 0.427 \left(\frac{\lambda}{5000} \right)^{3.7}, \quad (14)$$

where the observed wavelength $\lambda = c/\nu$ with the speed of light c . This mean intergalactic optical depth is obtained by averaging the results from the Monte-Carlo simulation and matches the observed optical depths as shown in Figure 3.

The background fluctuation δ_ν^{back} is obtained from the sky-subtracted two-dimensional spectra. As described in the previous subsection, we identify spatially 10 pixels as the background region in each two-dimensional spectrum. Then, we calculate the root-mean-square (r.m.s.) spectrum of the sky-subtracted background from the 10 pixels, which we denote e_ν^{back} . A typical value of e_ν^{back} is $\approx 28 \text{ nJy}$ per one spatial pixel at 5000 \AA . Then, we draw δ_ν^{back} randomly from a Gaussian distribution with the mean of 0 and the standard deviation of $\sqrt{N_{\text{pix}}} \times e_\nu^{\text{back}}$, where $N_{\text{pix}} = 4$ is the number of the spatial pixels in the object spectrum extraction.

We have generated 15,000 mock observed spectra for each LBG. These mock spectra are processed by the same procedure as the real observed spectra described in section 3.1, and then, we obtain composite spectra. The distribution of the composite (normalized) flux densities in each wavelength element is well described by a Gaussian function around unity. Note that the spectra were normalized in the composite procedure, and then, the mean should be about unity by construction. The standard deviation of the distribution gives us an estimate of the uncertainty at each wavelength in the resultant composite spectrum. Figure 4 shows the breakdown of the contributions of the intergalactic absorbers and the background fluctuation to the standard deviation. We find that the background contribution is dominant.

In addition, we tried two other methods for estimating

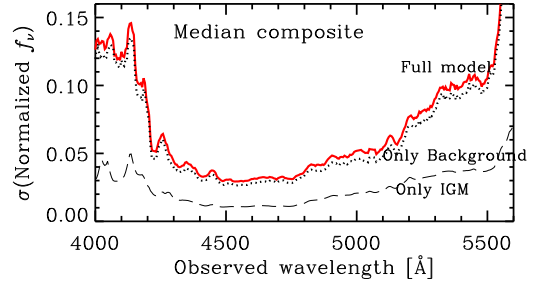


Figure 4. The standard deviation spectrum of the 15,000 observer’s frame median composite spectra generated by the Monte-Carlo simulation (solid line). Breakdown of the contributions of the sky-subtracted background (dotted line) and IGM fluctuations (dashed line) to the standard deviation.

f_ν^{cont} of equation (11): a linear continuum in the DA range and a power-law fit at longer wavelengths and an extrapolation to the DA range. The resultant standard deviation spectra were very similar to that of the constant case shown in Figure 4. In the following, we adopt the simplest constant DA case.

4 RESULT

We show in Figure 5 the resultant observer’s frame median composite spectrum. We also obtain a similar result from the 3-sigma clipping average composite. The displayed range is the wavelength where the number of LBGs used in the composite is larger than 7 as shown in the bottom panel. In the middle panel, the composite spectra are shown by the solid line, while the sky-subtracted background composite is shown by the dotted line. We can see larger fluctuations in the object composite than in the background composite, indicating the reality of these features in the object composite. The almost horizontal line around unity actually shows the mean of the 15,000 composites generated by the Monte-Carlo simulation. The standard deviation in each wavelength pixel of these simulated composites is shown by the dashed lines which are well matched with the fluctuation of the background composite. This is consistent with what we have seen in Figure 4; the background fluctuation dominates the fluctuation by random IGM absorbers.

The top panel shows the redshift distribution of the LBGs reported by Steidel et al. (2003) and our VI08 survey. The dashed line shows the expected number for a universe where LBGs were distributed uniformly, which is estimated from a number-weighted average of the selection functions of VI08 and Steidel et al. (2003) shown in Figure 2. We can find some spikes and voids in the distribution and the most prominent spike is the known PC at $z = 3.1$ (Steidel et al. 1998, 2000; Hayashino et al. 2004; Matsuda et al. 2004, 2005; Yamada et al. 2012a).

Very interestingly, we can see a strong dip in the object composite at the wavelength exactly corresponding to the PC H I Ly α . Furthermore, some peaks and dips in the object composite seem to correlate with voids and spikes in the LBG redshift distribution, respectively, especially at wavelengths longer than $4,800 \text{ \AA}$ or redshift $z > 2.95$. As described in equation (7), the observer’s frame composite

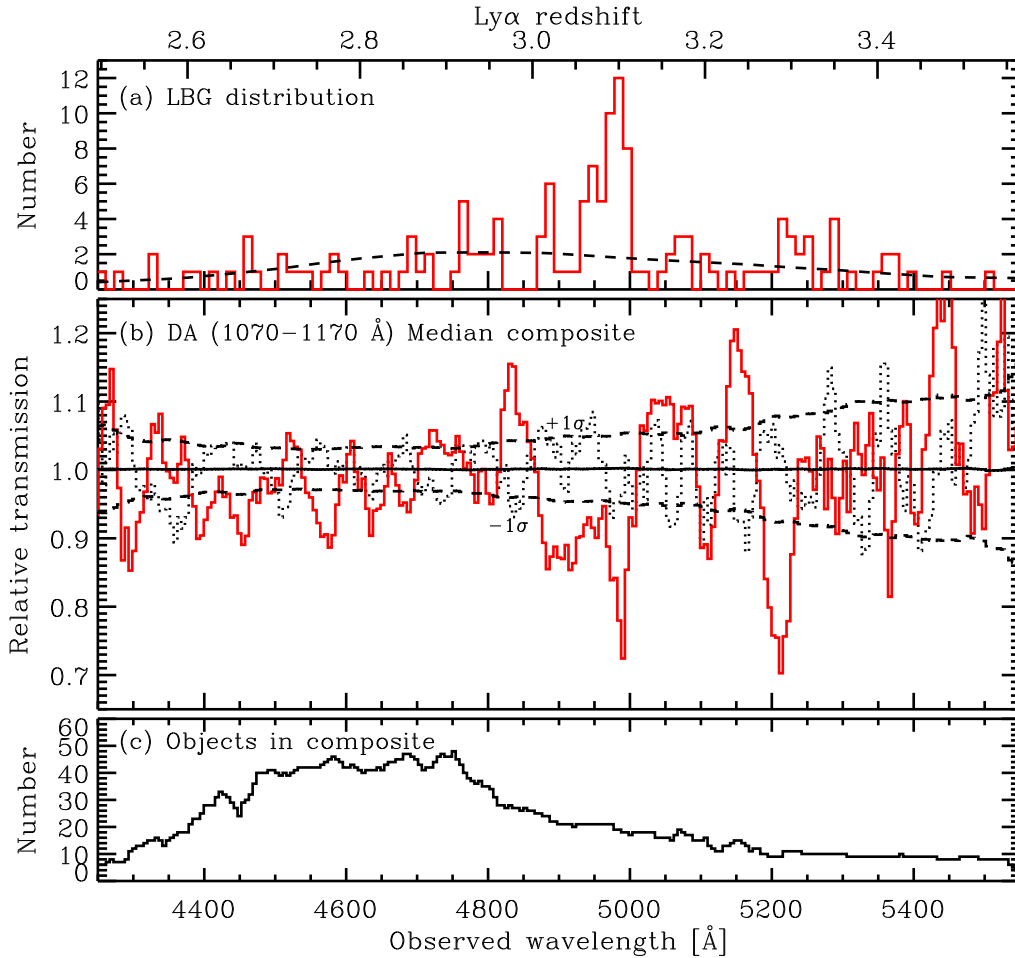


Figure 5. Observer’s frame composite spectrum of LBGs in the SSA22 field. (a) Spectroscopic redshift distribution of the LBGs whose redshifts are categorized as Ae, Aa and B from our VI08 observation and the LBGs from Steidel et al. (2003). The dashed line is the distribution expected when the galaxies distribute uniformly. (b) The IGM transmission relative to the mean. The dotted line is the composite of the sky-subtracted background. The almost horizontal solid line with the intercept at 1.0 and the dashed lines indicate the mean and $\pm 1\sigma$ for one pixel from a Monte-Carlo simulation of the composite procedure, respectively. (c) The number of objects used for the composite at each wavelength element.

obtained in this paper is equivalent to the IGM transmission spectrum normalized by its mean. Thus, the dip/peak of the object composite corresponds to more/less absorption in the IGM than the mean at that redshift.

In this paper, we focus on two sharp absorption dips which have the minimum transmission less than 0.8, together with two sharp transparency peaks greater than 1.15 in Figure 5. All dips and peaks selected are also required to have 10 or more sight-lines. Their redshifts are 3.10 and 3.28 for the dips as well as 2.98 and 3.24 for the peaks respectively. There is another interesting absorption dip around at $z = 3.04$, probably corresponding to the LBG density peak at the same redshift. As Topping et al. (2018) discussed, this LBG overdensity is another PC. However, the absorption dip is shallower but wider than those selected above. Therefore, we will defer to examine this feature until more data are available for this.

4.1 EWs and significance of the peaks and dips in the transmission spectrum

There is a significant fluctuation in the observer’s frame composite. This is equivalent to the fluctuation relative to the mean IGM transmission because we have normalized individual LBG spectra during the composite procedure. The intrinsic galaxy spectrum in the DA range which is used in the composites is smooth enough and can not produce such a fluctuation. To quantify the significance of the peaks and dips against the mean IGM transmission, we define the *excess* equivalent width (EW) as

$$EW_{\text{exc}} \equiv \sum_{\lambda_1 \leq \lambda \leq \lambda_2} (\tilde{f}_\lambda - 1) \Delta\lambda, \quad (15)$$

where \tilde{f}_λ is the normalized composite flux density⁴, $\Delta\lambda = 5.3 \text{ \AA}$ is the width of the wavelength element, and λ_1 and

⁴ $\tilde{f}_\lambda = f_\lambda / f_\lambda^{\text{cont}} = f_\nu / f_\nu^{\text{cont}} = \tilde{f}_\nu$ which is the obtained composite spectrum and the IGM transmission fluctuation divided by the mean transmission as described in equation (7),

λ_2 are the lower and upper wavelength boundaries to be summed up as a feature, respectively. Then, let us define two different uncertainties for EW_{exc} based on the standard deviation spectrum obtained by the Monte-Carlo simulation, $\sigma_{\text{MC},\lambda}$. Note that $\sigma_{\text{MC},\lambda}$ is non-dimensional. One is the case without any correlation in the wavelength space:

$$\sigma_{\text{noncor}}^{EW} = \sqrt{\sum_{\lambda_1 \leq \lambda \leq \lambda_2} \sigma_{\text{MC},\lambda}^2 \Delta\lambda^2}. \quad (16)$$

The other is the case with a complete correlation in the wavelength space:

$$\sigma_{\text{cor}}^{EW} = \sum_{\lambda_1 \leq \lambda \leq \lambda_2} \sigma_{\text{MC},\lambda} \Delta\lambda. \quad (17)$$

In the Monte-Carlo simulation, we have assumed neither correlation of IGM absorbers nor correlation of the background fluctuation along wavelength (or redshift). However, there should be a redshift correlation of IGM absorbers (e.g., Zuo & Bond 1994; Cristiani et al. 1995; Meiksin & Bouchet 1995; Croft et al. 1999; McDonald et al. 2000). Thus, $\sigma_{\text{MC},\lambda}$ tends to underestimate the fluctuation in the real Universe. In this sense, the former, non-correlated uncertainty, $\sigma_{\text{noncor}}^{EW}$ would result in an underestimation. On the other hand, the latter, completely correlated uncertainty, σ_{cor}^{EW} would result in considerable overestimation when the background noise is random and dominates $\sigma_{\text{MC},\lambda}$. We do not know how much the absorbers' correlation enhances their contribution in $\sigma_{\text{MC},\lambda}$ quantitatively, at the moment, while the contribution is minor in the no absorbers' correlation case, as seen in Figure 4. In summary, the real uncertainty should be bracketed by these extreme cases. Then, we define the two S/N ratios for EW_{exc}

$$(S/N)_{\text{max}} = \frac{|EW_{\text{exc}}|}{\sigma_{\text{noncor}}^{EW}}, \quad (18)$$

and

$$(S/N)_{\text{min}} = \frac{|EW_{\text{exc}}|}{\sigma_{\text{cor}}^{EW}}, \quad (19)$$

as the *maximum* and *minimum* S/N ratios, respectively.

For the four dips and peaks in the transmission spectrum selected above, the significance by equation (18) and (19) are summarized in Table 3 for each case of median and (3- σ clipping) average composites. We have measured their *excess* EWs defined by equation (15) by adopting a bootstrap method (e.g., Press et al. 1992); before the step (iii) in the composite procedure described in section 3.1, we insert one step of random resampling of the normalized DA spectra with duplication. Then, we repeat the process 10,000 times. In this estimation, the wavelength range of the each dip/peak (from λ_1 to λ_2) is fixed to the range determined to cover the whole structure of the dip/peak in the observed composite shown in Figure 5. The resultant *excess* EWs, 1 σ errors and the wavelength ranges are summarized for the four dips and peaks in Table 4. In the next subsection, we investigate their dips and peaks in detail.

4.2 Prominent peaks and dips in the transmission spectrum

4.2.1 $z = 3.10$ absorption dip

This absorption dip found at exactly the same redshift as the PC in the observing field is the most significant one detected ($\gtrsim 4\sigma$). In Figure 6, we show the spatial distribution of the sight-lines contributing to the dip feature in the composite as the cross marks. We also plot the positions of LBGs within the redshift range corresponding to the dip feature ($3.07 < z < 3.12$) taken from the catalogs by our VIMOS survey and Steidel et al. (2003), and the surface number density contour of LAEs at $z = 3.06$ – 3.13 by Yamada et al. (2012a). These LAEs are selected with a narrowband filter in Hayashino et al. (2004) and its redshift coverage exceeds the lower redshift boundary of the dip feature, but most of the spectroscopic redshifts of the LAEs are around $z = 3.09$ (Matsuda et al. 2004). The positions of the LBGs seem to match with the LAE contour well, indicating that they are residing in the same structure at $z = 3.1$. The sight-lines are distributed over the LSPC in the Sb1 field, then, they are probing the “intra-LSPC” medium.

Let us examine the H I absorption enhancement as a function of the galaxy density. Although the number of sight-lines is not very large, we have divided the sight-lines into three subsamples depending on the LAE overdensity δ_{LAE} reported by Yamada et al. (2012a) at the positions of the sight-lines. Then, we have made their observer's frame composites and measured the *excess* EWs. In this analysis, we have kept the same wavelength range to measure the EW as that in Table 4. The results are summarized in Table 5. We find a weaker *excess* EW for the lowest δ_{LAE} subsample. However, it is not conclusive because the S/N remains low due to the small number of sight-lines in the subsamples at the moment.

4.2.2 $z = 2.98$ transparency peak

This transmission peak is detected with a significance level of $\gtrsim 3\sigma$. Remarkably, we have no LBG within the redshift range of the transmission peak, while the expected number in a random distribution is 8.2, which is calculated from the dashed line in the top panel of Figure 5. A Monte-Carlo simulation tells us that the probability to have zero LBGs within the redshift range of $2.96 < z < 3.00$ is $\sim 0.03\%$. This strongly suggests that this is a significant galaxy void. It is remarkable that this transparency peak at $z = 2.98$ indicating weaker Ly α absorption corresponds to the galaxy void besides the PC at $z = 3.1$. It is also important that the Ly α absorption in this void is not zero because the IGM optical depth would be 0.24 for a mean transmission of 0.38 at the redshift (see eqs. 4, 8 and 14), indicating that there is substantial neutral hydrogen (or the LAF) even in a galaxy void, which is consistent with a result obtained in the low- z Universe ($z \lesssim 0.1$) (Tejos et al. 2012). Figure 7 shows the distribution of the background sight-lines.

4.2.3 Possible $z = 3.24$ transparency peak

As found in Table 3, this transmission peak is detected significantly in the two $(S/N)_{\text{max}}$ cases, but it is less than 3σ

Table 3. A summary of significance of the peaks and dips in the transmission spectrum.

Redshift peak/dip	Median		Average	
	$(S/N)_{\min}^a$	$(S/N)_{\max}^a$	$(S/N)_{\min}^a$	$(S/N)_{\max}^a$
2.98 peak	2.86 (5pix)	6.64 (7pix)	4.00 (5pix)	9.31 (9pix)
3.10 dip	3.84 (5pix)	8.98 (11pix)	4.39 (5pix)	9.81 (5pix)
3.24 peak	2.91 (5pix)	6.91 (7pix)	2.73 (5pix)	6.12 (7pix)
3.29 dip	3.26 (5pix)	7.98 (7pix)	1.81 (5pix)	4.56 (9pix)

^a See the definitions of equations (18) and (19). The number in the parenthesis is the integrated pixels used in the S/N calculations.

Table 4. Properties of the peaks and dips in the transmission spectrum.

Redshift peak/dip	Wavelength [Å]	Fiducial range		Number of pixels	Number of sight-lines	Number of LBGs ^a	EW_{exc} [Å] ^b		Remarks
		λ_1 [Å]	λ_2 [Å]				(Median)	(Average)	
2.98 peak	4836.5	4820.6	4863.0	9	30	0 (8.2)	4.3 ± 2.1	7.0 ± 2.0	Void
3.10 dip	4984.9	4963.7	5006.1	9	21	34 (7.1)	-7.0 ± 2.3	-7.1 ± 2.0	Proto-cluster
3.24 peak	5154.5	5128.0	5175.7	10	17	2 (6.3)	6.3 ± 3.5	5.3 ± 2.6	Void?
3.29 dip	5207.5	5181.0	5234.0	11	12	12 (6.2)	-7.3 ± 7.3	-5.5 ± 4.9	Overdensity?

^a The number in the parenthesis is an expectation from a random distribution of galaxies.

^b *Excess* equivalent width in the observer's frame defined by equation (15) measured by a bootstrap method.

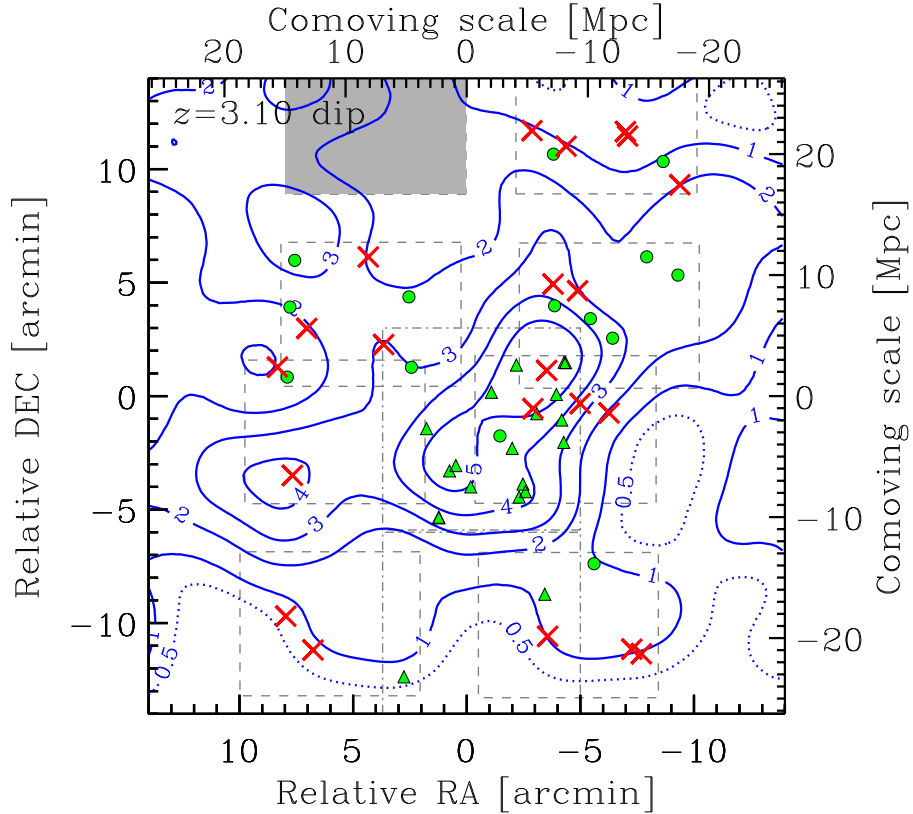


Figure 6. Spatial distribution of the sight-lines probing the IGM between $z = 3.07$ and $z = 3.12$ (cross marks). The circles and triangles are the LBGs whose redshifts are measured in the VI08 and Steidel et al. (2003) surveys, respectively, and are within the redshift range. The contour shows the surface number density map of LAEs at $z = 3.06$ – 3.13 by Yamada et al. (2012) and Hayashino et al. (2004). The numbers along the contours indicate the density enhancement factor relative to the mean surface number density of LAEs in general fields at $z = 3.1$: $n_{\text{LAE}}/\langle n_{\text{LAE}} \rangle$. The gray dashed and dot-dashed lines show the fields-of-view of VI08 and Steidel et al. (2003) observations, respectively. The shaded north-east part is the unavailable quadrant of VI08 (see section 2.2).

Table 5. Dependence of $z = 3.10$ IGM absorption dip on LAE overdensity and angular distance to the nearest *spectroscopic* LBG.

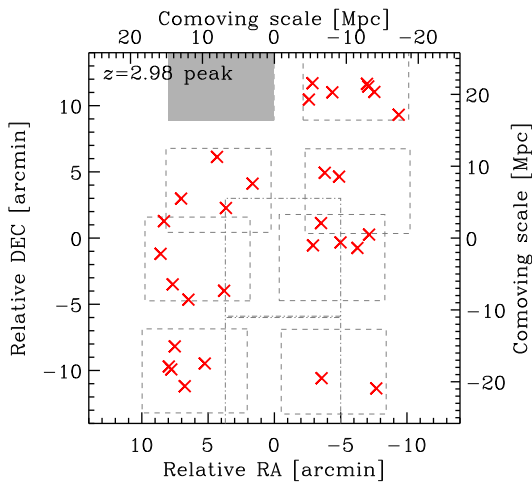
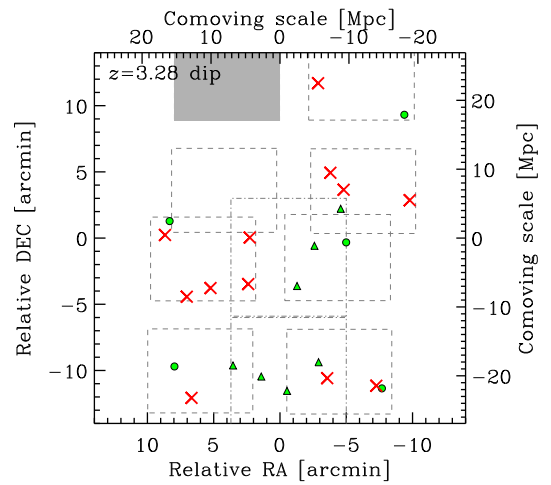
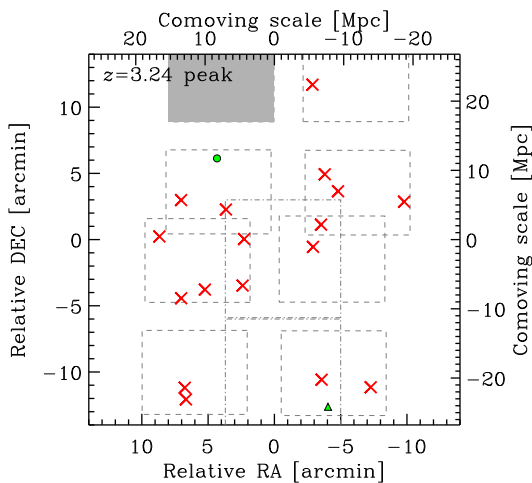
Subsample	N_{SL}^a	$\langle \delta_{\text{LAE}} \rangle^b$	$\langle d_{1,\text{LBG}} \rangle^c$ [arcmin]	$EW_{\text{exc}}^{\text{rest}} [\text{\AA}]^d$ (Median)	$EW_{\text{exc}}^{\text{rest}} [\text{\AA}]^d$ (Average)
All	21	1.19	1.98	-1.7 ± 0.6	-1.7 ± 0.5
$\delta_{\text{LAE}} \geq 1$	7	3.14	1.13	-2.1 ± 1.4	-2.3 ± 1.1
$0.03 \leq \delta_{\text{LAE}} < 1$	7	0.56	1.80	-2.2 ± 1.1	-2.3 ± 1.0
$\delta_{\text{LAE}} < 0.03$	7	-0.12	3.00	-0.9 ± 0.8	-1.2 ± 0.8

^a Number of sight-lines.

^b Average of the LAE overdensities at the positions of the sight-line, where $\delta_{\text{LAE}} = n_{\text{LAE}} / \langle n_{\text{LAE}} \rangle - 1$.

^c Average angular distance to the nearest *spectroscopic* LBG from each sight-line.

^d Rest-frame *excess* equivalent width defined by equation (15) measured by a bootstrap method.


Figure 7. The spatial distribution of the sight-lines between $z = 2.96$ and $z = 3.00$. The gray lines and shaded area are the same as in Figure 6.

Figure 9. Same as Figure 8 but for the sight-lines between $z = 3.26$ and $z = 3.31$.

Figure 8. Same as Figure 7 but for the sight-lines between $z = 3.22$ and $z = 3.26$. The LBGs in the redshift range are shown by the same symbols as in Figure 6. The FoVs are also shown as in Figure 6.

in both the $(S/N)_{\text{min}}$ cases. Then, we consider this peak as a possible detection. The number of LBGs within the feature is 2 against an expectation of 6.3. A Monte-Carlo simulation predicts a probability less than 5% for 2 or a smaller number of LBGs in this redshift range, and thus, it is a possible LBG void ($\sim 1.6\sigma$). However, we have to reserve a definite conclusion about the reality of this peak until more data become available. Figure 8 shows the distribution of the LBGs and sight-lines.

4.2.4 Possible $z = 3.28$ absorption dip

This absorption dip is significantly detected in the median composite but not in the $3\text{-}\sigma$ clipping average composite as found in Table 3. Then, we consider this feature as a possible detection. On the other hand, there is an overdensity of LBGs at $3.26 < z < 3.31$ corresponding to the dip feature; the number of LBGs is 12 against a random expectation of 6.2. A Monte-Carlo simulation tells us the probability to have more than or equal to 12 LBGs within this redshift range to be 2%, corresponding to a significance level of $\sim 2\sigma$. Figure 9 shows the spatial distribution of LBGs which seem to cluster at the south-east quarter of the field. Unfortunately, the IGM probing sight-lines do not distribute inside of the LBG structure but do around it. This spatial

displacement probably reduces the significance of the IGM transmission feature, if real. Clearly a much larger number of spectra is required to reveal the nature of this dip.

4.3 Cross-correlation between galaxies and H I transmission

We consider here the cross-correlation between the H I transmission spectrum and the LBG redshift distribution defined as follows to evaluate the degree of their synchronization. First, a spectrum expressing significance of the H I fluctuation can be defined as

$$\epsilon_\lambda \equiv \frac{\tilde{f}_\lambda - 1}{\sigma_{MC,\lambda}}, \quad (20)$$

where \tilde{f}_λ is the normalized composite spectrum and $\sigma_{MC,\lambda}$ is the standard deviation in each wavelength element estimated by our Monte-Carlo simulation. Next, we define a spectrum describing the LBG overdensity significance as

$$\delta_{z(\lambda)} \equiv \frac{n_{z(\lambda)}^{\text{obs}} - n_{z(\lambda)}^{\text{exp}}}{\sigma_{\text{LBG},z(\lambda)}}, \quad (21)$$

where $n_{z(\lambda)}^{\text{obs}}$ and $n_{z(\lambda)}^{\text{exp}}$ are, respectively, the observed and expected numbers of the LBGs in the redshift z interval corresponding to the wavelength element $\Delta\lambda$ of the VIMOS setting used in our VI08 survey, and the uncertainty $\sigma_{\text{LBG},z(\lambda)}$ can be expressed as

$$\sigma_{\text{LBG},z(\lambda)}^2 \approx \sigma_{\text{obs},z(\lambda)}^2 + \sigma_{\text{exp},z(\lambda)}^2, \quad (22)$$

where $\sigma_{\text{obs},z(\lambda)}$ is given by a small number Poisson statistics with the parameter $n_{z(\lambda)}^{\text{obs}}$ (Gehrels 1986)⁵ and $\sigma_{\text{exp},z(\lambda)} \approx \sqrt{n_{z(\lambda)}^{\text{exp}}}$ as also expected by the Poisson statistics, which we have confirmed by a Monte-Carlo simulation. Finally, we define the cross-correlation coefficient as

$$\xi_{\text{cc}} \equiv \frac{1}{n} \sum_{i=1}^n \epsilon_{\lambda_i} \delta_{z(\lambda_i)}, \quad (23)$$

where λ_i is the i th wavelength element and n is the total number of wavelength elements used in the calculation. We restrict ourselves to the wavelength elements where the number of the spectra used in the composite is equal to or larger than 7 as in Figure 5. The resultant coefficients are -0.218 and -0.235 for the median and average composites, respectively.

For a comparison, we have performed an extensive Monte-Carlo simulation of the IGM transmission and of the LBG redshift distribution. We have 15,000 mock IGM composite spectra generated by the Monte-Carlo simulation as described in section 3.3. The simulation of the LBG redshift

⁵ The Poisson distribution with the parameter being a small number is asymmetric. Gehrels (1986) gives upper and lower 84-percentiles. Since we need a single value for $\sigma_{\text{obs},z(\lambda)}$, we use simple average values of the upper and lower percentiles. This choice determines the absolute value of the overdensity significance and the resultant cross-correlation coefficient. To evaluate the significance of the observed cross-correlation coefficient, however, we do not need the absolute value of the coefficients but need a relative comparison between the observational and random ones. Therefore, this choice does not affect our evaluation of the significance of the cross-correlation.

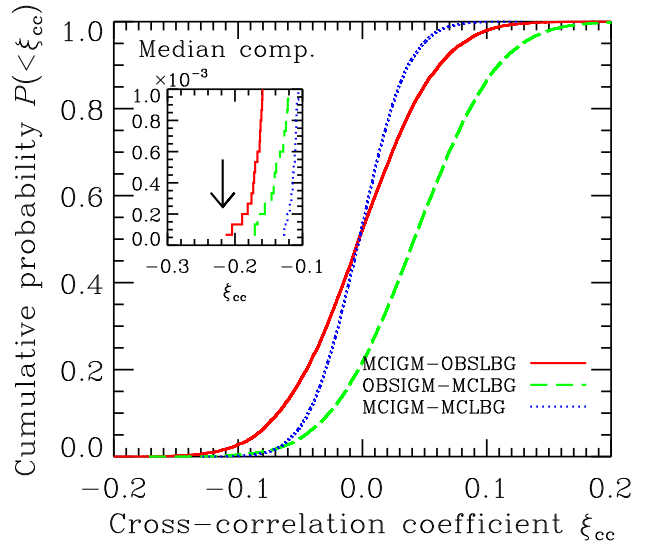


Figure 10. Cumulative probability distribution to have a value of the cross-correlation coefficient defined by equation (23) smaller than that in the horizontal axis for the median composite case. The solid line is the case with the combination of the Monte-Carlo IGM transmission and the observed LBG redshift distribution, the dashed line is the case of the combination of the observed IGM transmission and the Monte-Carlo LBG redshift distribution, and the dotted line is the case of the combination of both Monte-Carlo simulations. The inset is a zoom-in around the coefficient from the observed IGM transmission and the observed LBG redshift distribution indicated by the downward arrow.

distribution is based on the expected redshift distribution of the randomly distributed LBGs as shown in the top panel of Figure 5. Since we have 171 LBG redshifts, we randomly draw 171 redshifts from the expected function and repeat it 15,000 times. Then, we calculate the cross-correlation coefficient, ξ_{cc} , from these 15,000 sets of the IGM transmission and the LBG redshift distribution. We try three combinations of them: (1) the Monte-Carlo IGM and the real LBG redshift, (2) the real IGM composite and the Monte-Carlo LBG redshift, and (3) both data from the Monte-Carlo simulations. Figure 10 shows the cumulative probability function to have a coefficient ξ_{cc} smaller than the value in the horizontal axis for the median composite. We find that the observational coefficients noted at the end of the previous paragraph are very rare in our Monte-Carlo simulation: $< 2 \times 10^{-5}$ and 7×10^{-5} for the median and average composites, respectively. Assuming a Gaussian distribution, these values correspond to > 4.1 - and 3.8 - σ excesses, respectively.

Negative values of the cross-correlation coefficient mean an anti-correlation of the IGM transmission and the LBG redshift distribution, namely, an enhanced (reduced) Ly α absorption in a galaxy overdensity (underdensity). Since the negative values of the coefficient obtained from the observed data are extremely difficult to be explained with random distributions of the IGM and LBGs, we conclude that the IGM transmission significantly anti-correlates with the LBG distribution.

From Figure 10, one can appreciate a bias towards positive values found in the combination of the observed IGM transmission and the Monte-Carlo LBG distribution (the

Table 6. A summary of significance of each correlation.

Redshifts	median σ	average σ
full z range ($z = 2.46 - 3.55$)	> 4.1	3.8
$z2.98$ peak ($z = 2.97 - 3.00$)	3.7	> 4.1
$z3.10$ dip ($z = 3.07 - 3.12$)	3.9	4.1
$z3.24$ peak ($z = 3.22 - 3.26$)	2.3	2.3
$z3.28$ dip ($z = 3.26 - 3.31$)	2.3	2.0
all z except $z3.10$ dip	3.1	2.8
all z except $z3.10$ dip & $z2.98$ peak	1.9	1.5

dashed line in Figure 10). This is because the observed IGM fluctuation ϵ_λ and the Monte-Carlo LBG overdensity $\delta_{z(\lambda)}$ are both biased towards negative values. Since we calculate $\delta_{z(\lambda)}$ in the wavelength pixel scale of our VIMOS spectroscopy and the numbers of LBGs in many pixels are then zero, resulting in negative $\delta_{z(\lambda)}$. In fact, the mean of $\delta_{z(\lambda)}$ from the observed LBG distribution is also negative and very similar to those from the Monte-Carlo simulation. On the other hand, the Monte-Carlo IGM fluctuation gives a very symmetric distribution around zero. This is the reason why we have obtained a median value of ξ_{cc} close to zero with the Monte-Carlo IGM in Figure 10. The observed IGM ϵ_λ tends to be negative: more Ly α absorption as seen in the previous subsections.

We summarize correlation significance for each redshift range in Table 6. The high significance of the full redshift range described above is recognized to be a result of strong correlations mainly at $z = 3.1$ and 2.98.

5 DISCUSSION I: THE LARGE-SCALE PROTO-CLUSTER AND SURROUNDINGS

5.1 Cosmological characteristics of the large-scale proto-cluster

In the beginning of the discussion, we estimate the total mass and a finding probability of the LSPC in the SSA22 field at $z = 3.1$, which has induced the present spectroscopic survey, based on the LAE overdensity and an assumed bias parameter, amplitude of galaxy overdensities versus those of matter. Here, we precisely define the LSPC as the area in the SSA22 Sb1 field where the local LAE number density exceeds 1.5 times the mean value of the control fields, i.e., 0.204 LAEs arcmin $^{-2}$ obtained in Yamada et al. (2012a). The contours expressing the LSPC area, the high density region (HDR) of the LAE is displayed in that article. The HDR contains 259 confident LAEs defined in Yamada et al. (2012a) and 35 LABs including two gigantic ones by Steidel et al. (2000), which would be considered to be progenitors of massive galaxies in the present Universe, as well as around 50 LAAs, a number of LBGs and K-band selected galaxies (Uchimoto et al. 2012). So, the HDR is becoming to be called the ‘‘large-scale proto-cluster (LSPC)’’. The FoVs of our VIMOS survey have been set up to probe the LSPC.

The LAE number density of the LSPC is 0.58 arcmin $^{-2}$, i.e., the overdensity δ of the LAE is 1.89 ± 0.18 , which can be translated to the underlying matter overdensity of $\delta_M = 0.99 \pm 0.25$, if we adopt the linear bias parameter of $b_{LAE} = 1.9_{-0.5}^{+0.4}$ for the LAE. This value was taken

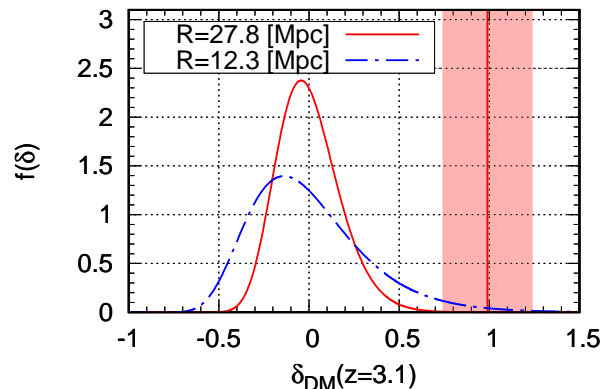


Figure 11. The probability distribution function (PDF) of the dark-matter mass overdensity δ_{DM} at $z = 3.1$, as a result of the cosmological evolution of the initial Gaussian mass fluctuation, within a sphere having the radius of 27.8 comoving Mpc is shown by the solid curve. The dot-dashed curve is the case with a radius of 12.3 comoving Mpc for a comparison. The vertical solid line and shaded region are, respectively, δ_{DM} and its uncertainty for the $z = 3.1$ LSPC in the SSA22 field.

from Guaita et al. (2010) (see also Gawiser et al. 2007) for $z \simeq 3$ LAEs and would be reasonable compared to $b = 2.6$ (Bielby et al. 2013) assumed in Cucciati et al. (2014) for the LBGs at $z = 3$. The comoving volume of the LSPC is 0.92×10^5 Mpc 3 indicating a radius of $R = 27.8$ cMpc (comoving Mpc) of a corresponding spherical volume, for which a 1- σ mass fluctuation is estimated to be $\sigma_M = 0.12$ at $z = 3.1$ from the linear growth theory of CDM mass fluctuations with the normalization $\sigma_8 = 0.81$, in the same manner as Yamada et al. (2012a). This means the probability of the LSPC amounts to $8.3 \pm 2.1 \sigma$, i.e., around 10^{-10} . Although the volume of the LSPC is very large, the effect of the gravitational evolution such as the gravitational contraction of the massive structure should be taken into account to obtain the probability accurately. We evaluated it by the method of Mawatari et al. (2012) who used the log-normal probability distribution function (PDF) of underlying mass fluctuations as a reference. In the calculation of the PDF, the gravitational contraction of the structure and the effect of redshift distortion, the so-called Kaiser effect (Kaiser 1987) were taken into account. We estimated the PDF for mass fluctuations within the spherical region with a radius of $R = 27.8$ cMpc at $z = 3.1$ (see Figure 11). From the function, we obtain the appearance probability of $0.0023_{-0.0022}^{+0.0483} \%$ for the LSPC with the mass overdensity of $\delta_M = 0.99 \pm 0.25$. The probability is considerably larger than the estimate from the simple linear growth theory described above. It appears that the LSPC with the extremely large total mass of $\approx 0.90 \times 10^{16} M_\odot$ has already begun the gravitational contraction at $z = 3.1$.

5.2 H I transparency peaks close by the large-scale proto-cluster

We have detected two significant correlations between LBGs and H I transmission with 4σ or more at $z = 3.10$ and 2.98, together with two possible ones at $z = 3.24$ and 3.28 with about 2σ significance, in the previous section. We call

redshift coincidences between LBG-HDR and the absorption dip in Figure 5, “Counter-Balance structure 1, CB1” as well as the ones between the LBG low density region (LDR) or void and transparency peak in the figure, “CB2”, respectively. In this subsection, we discuss CB1 at $z = 3.10$ and CB2 at $z = 2.98$ having sufficient significance, qualitatively, and briefly mention the simultaneous appearance of two transparency peaks at $z = 2.98$ and 3.24 .

The CB1 is not too difficult to be understood, because high density LBGs and their H I halos absorb photons at the Ly α wavelength with high probabilities. H I gas proper to the LBG cluster may also contribute to make a dip, as suggested in Mawatari et al. (2017). On the other hand, the CB2, the high transparency peak seen in the transmission spectrum at the LBG void or LDR, is not so easy to be interpreted. As the simplest interpretation, in a void/LDR, absence or underdensity of LBGs with H I halos would cause such transparency in H I. It is valid, if the Ly α depression is caused mainly by LBGs and their H I halos. However, this picture does not seem to be true. For example, we can find LBG-LDRs without transmission peaks at $z = 2.80$ and 2.90 in Figure 5. For the former LDR, the number of LBGs detected at redshifts between $z = 2.79$ and 2.84 is only two, against 9.7 LBGs expected in the uniform distribution shown by the dashed line in Figure 5 (a). A Monte-Carlo simulation gives the probability of around 0.3% to have two or a smaller number of LBGs in this redshift range, implying the $z = 2.80$ is an LBG void with $\sim 3\sigma$ significance. However, any transparency peak is not seen at all at the redshift in the transmission spectrum in Figure 5 (b), despite a lot of sight-lines. The narrow LDR at $z = 2.90$, where one LBG is found at $2.89 \leq z \leq 2.91$ whose probability is estimated at 5.6% ($\sim 1.6\sigma$), also exhibits no transparency peak. This could mean that a significant fraction of HI absorption in these regions is not directly associated to galaxy halos (e.g. Tejos et al. 2012 for a similar conclusion at low redshifts).

At redshifts lower than $z = 2.8$, from $z = 2.75$ down to 2.55 , it is difficult to discuss the LBG redshift distribution and identify voids/LDRs with sufficient significance because the LBG detection efficiency in their redshifts is low as indicated by the dashed line in Figure 5 (a). The CFHT u^* -band used in our LBG selection to detect dropout phenomena has a relatively long central wavelength and the lower bound of the selection redshift becomes relatively high. On the other hand, the VIMOS sensitivities are not too low to measure the spectra at wavelengths between 4300 \AA and 4600 \AA , corresponding to $z = 2.55$ – 2.75 in Ly α , and the composite transmission spectrum consists of a lot of sight-lines as shown in Figure 5 (c). So, in this redshift range, we can perform H I transmission measurements with sufficient significance. According to the cosmological simulations such as the Millennium simulation (Springel et al. 2005), there should be several LBG voids/LDRs with the sizes of dozens of cMpc at redshifts between $z = 2.55$ and 2.75 (see also Stark et al. 2015b). We call them, which are expected at those redshifts but difficult to be recognized in our LBG survey, potential voids/LDRs. It is important that the observed voids/LDRs at $z = 2.80$ with $\sim 3\sigma$ and $z = 2.90$ with $\sim 1.6\sigma$ as well as potential ones at redshifts less than 2.75 make no transparency peaks at all as seen in Figure 5 (b). Therefore, absence or underdensity of LBGs in the ordinary void itself

does not seem to cause such a prominent transparency peak found at $z = 2.98$.

To understand the generation of the transparency peak at $z = 2.98$, we put an attention to the structure $\sim 100 \text{ cMpc}$ away along the line-of-sight: LSPC at $z = 3.10$ having large overdensities of LBGs and LAEs studied in the previous subsections. The LSPC defined in the SSA22 Sb1 field is considered to have the total mass of $\approx 0.90 \times 10^{16} M_{\odot}$ including the overdensity mass of $0.45 \times 10^{16} M_{\odot}$ ($\delta_M = 0.99$) under the assumption of a bias parameter of 1.9 for LAEs as discussed above. This extremely large overdensity will attract the matter from the regions surrounding the LSPC, decrease the matter density there, and accelerate the expansion of their space by so-called “tidal force”. If some regions of the surroundings have already been low density compared with the mean at an early epoch as a result of the hypothesized quantum fluctuation during the inflation, the region will effectively grow into a *real void*, i.e., devoid of galaxies and H I gas, under the strong gravity of the “nearby” massive LSPC, after the t_{eq} , the moment when the matter energy density just exceeds the radiation one. Even if the region did not exhibit a very low density fluctuation with a high σ , the tidal force induced by the “nearby” massive structure would accelerate a growth of the region into a sufficient void with less LBGs. Such an extended space will also cause a low LAF density on sight-line. In this way, the CB2 structure seen at $z = 2.98$, the LBG void associated with the H I transparency peak, would only be formed with a help of a nearby massive structure such as the LSPC at $z = 3.1$. We can test this hypothesis by finding more extreme high-density regions and hypothesizing that there should be voids of type CB2 nearby these structures too.

Moreover, in the panoramic survey for seven S-Cam FoVs, Sb1-7 in SSA22, very interestingly, more HDRs, defined as the area where the local LAE number density exceeds 1.5 times of the mean of the control fields, are found in Sb2-7 besides the LSPC in Sb1. The contours of their HDRs are displayed in the panoramic sky map in Yamada et al. (2012a). The total mass of these HDRs in the panoramic survey amounts to $3.2 \times 10^{16} M_{\odot}$ including the LSPC in Sb1, of which the overdensity mass is estimated to be $1.5 \times 10^{16} M_{\odot}$ with $b = 1.9$ for LAEs at $z = 3.1$. This huge overdensity mass will work as a source of the “tidal force” as discussed in the following.

Here, we have to consider that these overdensity masses obtained from the NB survey are limited to the space sliced by the NB filter whose thickness is 58 cMpc . So, it is only a part of the entire overdensity mass responsible to the tidal force for the space around $z = 2.98$, although it is already huge: $1.5 \times 10^{16} M_{\odot}$. We need the three-dimensional structures and overdensity map at least for the region within a radius of 100 cMpc around the LSPC at $z = 3.1$. Future wide-field spectroscopic surveys will provide the entire overdensity mass in this region to obtain the exact tidal force and accurately calculate the expansion of the surroundings of the LSPC.

In addition, a smaller concentration of LBGs between $z = 2.91$ and 2.96 can also contribute to the local space expansion at around $z = 3.00$. The structure, a modest HDR with a mean redshift of $z = 2.93$, has the overdensity of $\delta_{LBG} = 0.5$ compared with the dashed line for the uniform distribution in Figure 5 (a), which can be converted into

the mass overdensity of $\delta_M = 0.2$ by applying $b_{LBG} = 2.6$ (Bielby et al. 2013) previously used. Note that Steidel et al. (1998) found a damped Ly α (DLA) system at $z = 2.93$, suggesting the reliability of the overdensity of this modest ‘‘HDR’’. If we assume that the modest ‘‘HDR’’ has a spherical form with a diameter of 50 cMpc corresponding to the redshift interval of $dz = 0.050$ described above, the comoving volume becomes 6.5×10^4 cMpc³. Then, the overdensity mass of the modest HDR with $\delta_M = 0.2$ turns out to be $0.06 \times 10^{16} M_\odot$, which is about one-20th of the LSPC overdensity mass at $z = 3.10$. So, the gravity by the two sources is almost balanced at $z = 2.96$, the lower redshift edge of the $z = 2.98$ void. On the other hand, the gravitational force by the LSPC dominates the other edge at $z = 3.00$. In this way, the LSPC and probably associated HDRs around it should effectively expand the space between $z = 2.96$ and 3.00, to make both the LBG void and transparency peak at the redshift, i.e., CB2 structure.

Likewise, the transparency peak at $z = 3.24$ would be induced by the LSPC at $z = 3.10$ together with a modest HDR at $z = 3.28$ seen in Figure 5 (a), just behind the peak, with the same mechanism of the tidal expansion as the $z = 2.98$ peak formation.

5.3 Extended H I halo of LBGs

Using a large sample of foreground-background galaxy pairs, Steidel et al. (2010) revealed that LBGs have large H I halos from the composite spectra at the rest-frame of foreground galaxies. The H I halo extends to 0.3 proper Mpc (pMpc) corresponding to 1.2 cMpc at redshift 3 and 30 arcsec in the angular scale. For example, the rest-frame equivalent width of the H I amounts to around 0.3 Å at the impact parameter $b = 0.3$ pMpc. It can be said that their findings have changed the picture of galaxies at high redshifts. For QSO environments, Prochaska et al. (2013, 2014) presented remarkable radial profiles of H I and metal absorption of the circum-galactic medium of $z \sim 2$ massive galaxies hosting QSOs by using their sample of QSO pairs. Their findings also have changed the picture of QSO environment.

Following the studies on LBG halos by Steidel et al., Rakic et al. (2012) and Rudie et al. (2012) have found H I ‘‘halos’’ which extend to surprisingly large distances of around 2 pMpc, by using pairs of galaxy and background-QSO. Such an extension of a single galactic ‘‘halo’’ is quite strange, because 2 pMpc corresponding to 8 cMpc at redshift 3 is a typical scale of cluster of galaxies, i.e., it means that each LBG has an H I ‘‘halo’’ of the same extension as clusters of galaxies.

To understand the large H I ‘‘halo’’, it is important to look into the two-dimensional H I absorption map in the transverse and sight-line distances presented by Rakic et al. (2012) (see also Turner et al. 2014). H I at the impact parameter $b < 0.13$ pMpc shows the Finger-of-God, suggesting its virial motion in a galaxy, and H I at $b > 0.13$ pMpc exhibits the Kaiser effect (Kaiser 1987). The map indicates that H I at $b < 0.13$ pMpc clearly belongs to the host LBG, and H I at $b > 0.13$ pMpc can be interpreted as the falling cool gas to the LBG as pointed out in Rakic et al. (2012, 2013). If the LBG belongs to a cluster of galaxies, the falling cool H I would be supplied by the cluster. If it is a field galaxy, the H I is probably supplied by the intervening cos-

mic web around the LBG. Here, it is difficult to understand at present whether the falling H I gas is galactic medium or intergalactic. However, the virial H I gas of $b < 0.13$ pMpc clearly belongs to the LBG.

The PC at $z = 3.1$ in the SSA22 field has a large LBG overdensity, $\delta = 3$ for our VIMOS survey area. Therefore, the virial H I with $b < 0.13$ pMpc around the LBGs, which distribute in the cluster with a high density, may reproduce the observed excess absorption of $EW_0 = -1.7$ Å. In this case, there is no neutral hydrogen proper to the PC, which suggests that LBGs in the cluster are in a stage of the lack of fuel. On the other hand, there should be an H I supply to LBGs, if the virial H I can produce only a part of EW_0 of -1.7 Å. In a future work, we will use a Monte-Carlo method to study whether the virialized H I around LBGs in the PC is able to produce the observed EW_0 or not, taking into account contributions of faint LBGs.

6 DISCUSSION II : INHOMOGENEOUS STRUCTURES ACCOMPANIED WITH AGNS

It is generally recognized that LBG surveys using the U -dropout method are also effective for QSO/AGN detections at $z \sim 3$, because both spectra are usually similar in respect of the Lyman break in the U -band (Bielby et al. 2011). In fact, we detected 4 AGNs in VI08 and Steidel et al. (2003) also found two AGNs in this field in their $z \sim 3$ LBG survey. In addition, we identified 5 AGNs in our VIMOS survey carried out in 2006, VI06. It was 0.5 magnitude shallower than VI08 because of about half of the integration time of VI08 (Kousai 2011), and was not deep enough to detect LBGs having UV magnitudes fainter than around 25 AB. Therefore, we have not used VI06 data in the previous sections dealing with LBG spectra down to 25.4 AB. VI06 was a pilot observation for the VI08 LBG survey.

On the other hand, VI06 is deep enough to observe AGNs with UV continuum magnitudes brighter than 24.5 AB. LBG selection criteria of VI06 were similar to those of VI08 and both expected redshift histograms are thus similar: about uniform but slowly changing efficiency between $z = 2.7$ and 3.5 with a peak at $z = 3$ (see Figure 2 [a]).

In the following subsections, we discuss the nature of the AGN distribution and its number density, especially, the relation between AGN and LBG distributions at $z = 3$ –4 in the SSA22 field, using the AGNs from the three surveys described above. In Table 7, we present coordinates, redshifts, R magnitudes, and survey names of the 11 AGNs. We show the spectrum of an AGN from the VI06 survey with $z = 3.455$ as an example in Figure 12.

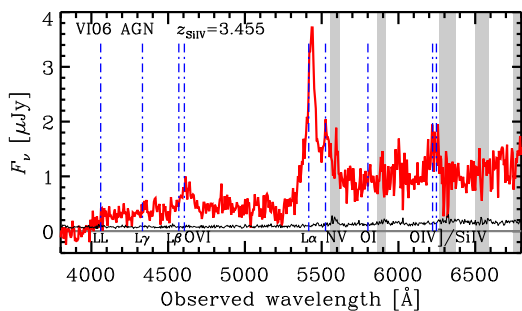
6.1 Extreme overdensity of AGNs at $z = 3.1$

It is remarkable that there are 5 AGNs with $R < 24.5$ in a narrow redshift range, $z = 3.084$ –3.132, where the LSPC and its envelope lie. We show the sky map of their AGNs with large green stars in Figure 13. Three of the five AGNs exist in the LAE density peak area.

The sky area they occupy is around $15' \times 8'$, i.e., 27×15 cMpc². The redshift difference of $dz = 0.05$ corresponds to about 45 cMpc. So, the number density of the

Table 7. List of 11 AGNs found in Steidel et al. (2003) and our VIMOS surveys.

Object	RA (J2000)	DEC (J2000)	Redshift	R [AB]	Survey
z2.42	22:17:04.87	+00:09:40.38	2.42	24.53	VI08
z2.50	22:18:31.36	+00:20:22.67	2.503	25.24	VI06
z3.084	22:17:36.51	+00:16:22.9	3.084	21.61	Steidel et al.
z3.091	22:17:16.23	+00:17:44.88	3.100	24.32	VI06
z3.104	22:17:09.62	+00:18:01.04	3.112	24.41	VI06
z3.112	22:17:12.60	+00:29:02.76	3.110	23.82	VI08
z3.132	22:17:06.75	+00:26:41.27	3.132	23.99	VI08
z3.353	22:17:22.26	+00:16:40.41	3.353	21.23	Steidel et al., VI06
z3.425	22:18:04.14	+00:19:46.88	3.425	24.62	VI08
z3.455	22:17:51.34	+00:20:36.66	3.455	22.87	VI06
z3.795	22:17:05.37	+00:15:14.25	3.801	22.01	VI06

**Figure 12.** One-dimensional spectrum of the AGN at $z = 3.455$. The Lyman limit system is seen at $z = 3.44$. The grey shaded regions indicate noisy wavelengths due to night emission lines. The vertical dot-dashed lines indicate some emission/absorption features.

AGN cluster is $5 \text{ AGNs} / 2 \times 10^4 \text{ cMpc}^3$. On the other hand, only 0.1 AGNs with $R < 24.5$ are expected in this volume from the QSO/AGN luminosity function (LF) for $z = 3.2$ by Masters et al. (2012). Even if we take a comoving volume of the entire LSPC, $1 \times 10^5 \text{ cMpc}^3$, the expected number of AGNs is 0.5.

It is noteworthy that about 4 AGNs with $R < 24.5$ are expected from their LF for our effective survey volume of $1 \times 10^6 \text{ cMpc}^3$, i.e., $z = 2.7\text{--}4.0 \times 322 \text{ arcmin}^2$. This is consistent with our three AGNs of $R < 24.5$ detected at $z = 2.7\text{--}4.0$ with the LBG selection criteria, except for the LSPC redshift. The extreme AGN concentration probably caused by the LSPC is a very interesting phenomenon to be intensively studied, in conjunction with overdensities of LBGs, LAEs, LABs and other kinds of objects in this field.

We also plot 6 $z = 3.1$ AGNs fainter than $R = 24.5$ from Micheva, Iwata, & Inoue (2017) with small stars in Figure 13. It is very interesting that the 11 AGNs in total form a filamentary structure along the LAE density peak. This structure at $z = 3.1$ could indicate important characteristics and dynamics on the formation mechanism and activities of AGNs. Future studies of the relation between the LSPC and AGNs as well as LBGs, LAEs, LABs, and so on, will offer us new insights on structure formation in the early Universe.

In contrast to our SSA22 survey, for example Bielby et al. (2011), in which about 1000 LBGs are identified in 10 times larger volume than ours, finds no remarkable

AGN concentrations as well as high density peaks of LBGs like the $z = 3.1$ LSPC.

In the following sections, we discuss the other 4 AGNs found behind the LSPC in the SSA22 field, apart from $z = 3.1$. Especially, correlations between AGNs and LBGs are considered.

6.2 “Sheet-like” structure of LBGs with an AGN at $z = 3.353$

The AGN at $z = 3.353$ is detected and spectroscopically measured by both Steidel et al. (2003) and VI06. The AGN has a DLA at $z = 2.93$ (Steidel et al. 2003). In a viewpoint of AGN-LBG correlation, we take notice of a modest LBG concentration consisting of 20 LBGs at $z = 3.28\text{--}3.37$ around the AGN’s redshift in Figure 5 (a). We show the sky map of these LBGs in Figure 14. Interestingly, the LBGs, except for the east-most one, form a filamentary structure in the redshift slice of $z = 3.28\text{--}3.37$, which extends along the north-south direction. The AGN lies at the center of the filament. Although the LBG redshift distribution for the entire FoV of 322 arcmin^2 in Figure 5 (a) may not show a strong evidence for an “LBG HDR”, the filamentary structure shown in Figure 14 supports the reality of the LBG high density.

Redshifts of the LBGs in the filament distribute almost uniformly between $z = 3.28$ and 3.36 , therefore the filamentary HDR in the two-dimensional sky map may be interpreted to be a sheet-like structure in the three-dimensional space having a narrow gap at $z = 3.33\text{--}3.34$ (see Figure 5 [a]). In addition, Mawatari et al. (2016) reported a DLA at $z = 3.335$ probably associated with this sheet-like structure, further enhancing the reality of the structure.

We discuss the overdensity and appearance probability of the HDR. The “sheet-like” HDR would be considered to have a mean width of 7 arcmin (13 cMpc) and a length of 27 arcmin (50 cMpc) in the sky plane represented in Figure 14, as well as the thickness of 75 cMpc corresponding to the redshift interval of the 19 LBGs, $dz = 3.370 - 3.283 = 0.087$. Thus, the comoving volume of the “sheet-like” HDR is $5 \times 10^4 \text{ cMpc}^3$, in which 6.0 LBGs brighter than $R = 25.4$ AB are expected when LBGs distribute uniformly, as the dashed line shows in Figure 5 (a). In this way, the HDR has a number overdensity $\delta_{\text{LBG}} = 2.2 \pm 0.7$, which results in a mass overdensity $\delta_M = 0.83 \pm 0.28$ when the bias parameter of $b = 2.6$ (Bielby et al. 2013) for LBGs is employed. On the other hand, the 1σ fluctuation of the dark matter for this

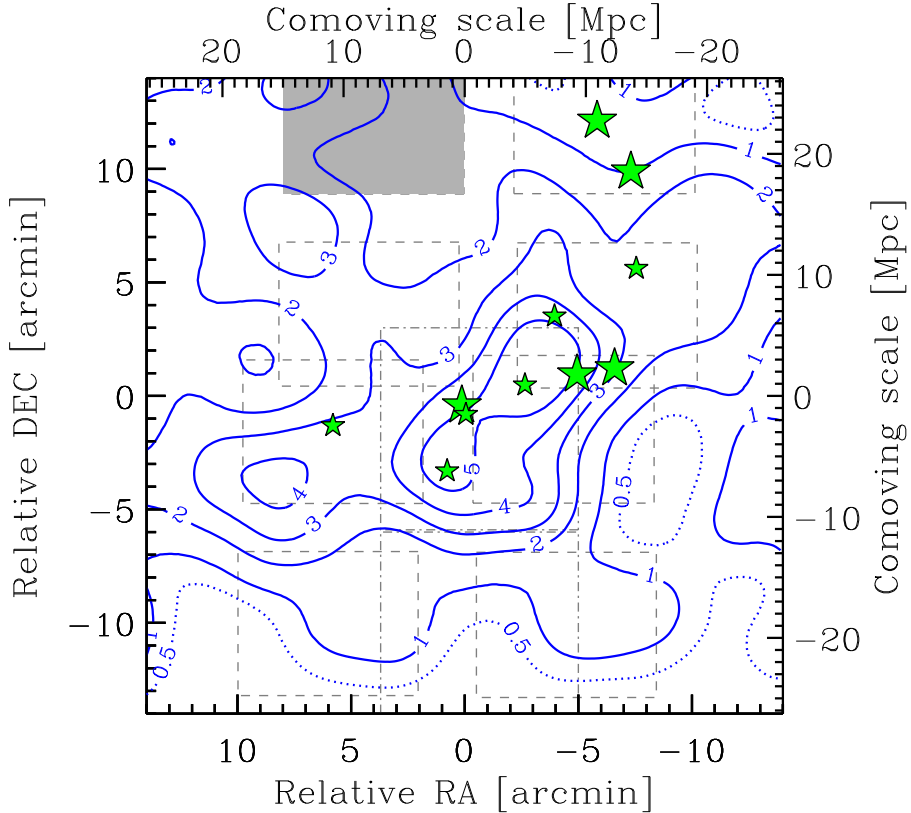


Figure 13. Sky distribution of 11 AGNs at $z = 3.084\text{--}3.132$. Large green stars are the AGNs with $R < 24.5$, and small green stars are ones with $R > 24.5$. The contours, grey lines and shaded area are the same as in Figure 6.

volume at $z = 3.33$ is estimated to be 0.124, according to the formula described in Yamada et al. (2012a). Then, this LBG HDR associated with the AGN at $z = 3.353$ is a rare event with the appearance probability of $7 \pm 2\sigma$.

6.3 Pair of AGNs around a dense H I cluster at $z = 3.453$

We detected a pairwise AGN at $z = 3.455$ and 3.425 with an angular distance of about 3 arcmin, whose spectra are shown in Figures 12 and 15 respectively. The former is a Type I AGN with $R = 22.87$, and the latter is a Type II AGN with $R = 24.62$, whose spectrum is very similar to the composite one for narrow-line AGNs in Hainline et al. (2011). We express the redshift of the pair with $z = 3.455$. The pair AGN does not seem to have any clusters of LBGs with the R -band magnitudes brighter than 25.4 AB around their redshifts in Figure 5 (a), although the detection efficiency for the LBGs is not so high at the redshifts. So, the AGNs may be interpreted as field objects independent of galaxy clustering. If our targets of the VI08 survey were only “objects” like galaxies in the ordinary survey, the pair would be misidentified as an isolated one in space. However, our survey can examine neutral hydrogen gas besides “objects”, as discussed in the previous sections. So, we investigate H I absorption dips around the pair of AGNs imprinted in DA ranges of spectra of background objects. Especially here, we search for H I gas clustering in the area within an angular radius of 10 arcmin

from the center of the pair, which corresponds to 20 cMpc at $z = 3.455$, a typical size of the PC at high redshifts.

In Figure 16, we show the sky map of the pair AGN together with sight-line positions of 10 background objects having redshifts of $z = 3.63\text{--}4.03$, whose DA ranges cover Ly α at $z = 3.425\text{--}3.455$. There are 5 sight-lines forming a “cluster” with a diameter of about 8 arcmin in the south part of the pair (the squares enclosing crosses in Figure 16). We have made a composite spectrum of the 5 sight-lines and show the result in Figure 17, which clearly shows a deep absorption dip with the rest-frame EW of about -5 \AA at 5415 \AA , corresponding to $z = 3.453$, if Ly α absorption is assumed. In contrast, the composite of the remaining 5 sight-lines shows no dips at the redshift as seen in Figure 17. Two of the 5 sight-lines in the “cluster of sight-lines” have very deep absorption dips like sub-DLA/Lyman limit systems (LLSs) at $z = 3.453$. Also the other 3 sight-lines have considerably significant dips at the redshift, indicating the dense H I gas at $z = 3.453$ extends over the entire 5 sight-line area with a diameter of at least 8 arcmin. We call the area a dense H I cluster (DHC).

Interestingly, the spectrum of the $z = 3.455$ AGN seems to have an LLS at 4050 \AA , i.e., $z = 3.441$ in Figure 12, indicating that there is plenty of H I gas also around the AGN. Therefore, the DHC found in the composite spectrum would not only cover the 5 sight-lines but also extend to cover the sight-line towards the $z = 3.455$ AGN. Here, we notice a slight difference between the Type-II AGN redshift, $z = 3.425$ and the composite dip one, $z = 3.453$ in Figure 17.

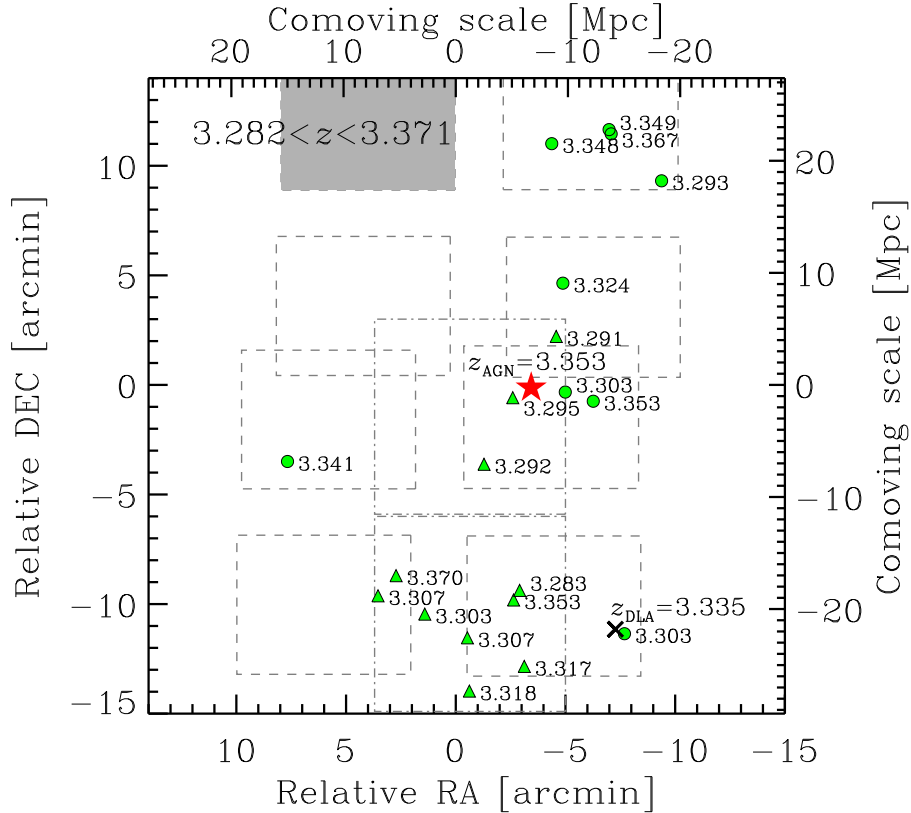


Figure 14. Sky distribution of 20 LBGs at $z = 3.28\text{--}3.37$. The green circles and triangles are the LBGs detected in the VI08 and Steidel et al. (2003) surveys, respectively. The numbers near the symbols indicate the redshift. The AGN at $z = 3.353$ is shown by the star symbol and the DLA at $z = 3.335$ is shown by the cross. The gray lines and shaded area are the same as in Figure 6.

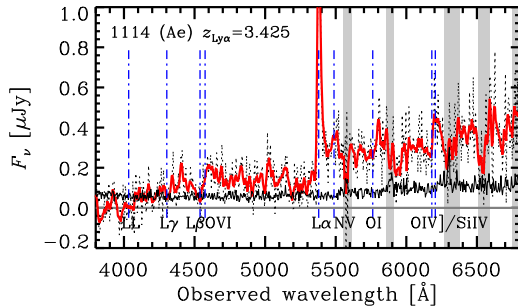


Figure 15. One-dimensional spectrum of the AGN at $z = 3.425$, which shows narrow emission lines. The gray shaded regions indicate noisy wavelengths due to night emission lines. The vertical dot-dashed lines indicate some emission/absorption features.

However, the nearest sight-line from the $z = 3.425$ AGN exhibits a considerable absorption feature down to $z = 3.40$ including the AGN redshift as shown by the blue dashed line in Figure 17, although the statistical significance is not high enough. Thus, the DHC has an angular diameter of at least about 10 arcmin and would have a three-dimensional structure extending to lower redshift around a sky position of the $z = 3.425$ AGN to include both AGNs as its members.

If the DHC spans the area of a 10 arcmin (or 20 cMpc) diameter (roughly 1/3 of the entire observing field) and the redshift range of $z = 3.420\text{--}3.470$, the expected number of

the $R < 25.4$ AB LBGs is 1.3 against no LBG in the area. Therefore, the pair AGN does not correlate with any LBG HDR. Nevertheless, it seems to be strongly associated with the DHC of a 20 cMpc scale. Such a relation is very interesting, even strange, and may be a new type of AGN-matter correlation. The rich H I gas in the 20 cMpc scale cluster should contribute to pair AGN generation and keeping their activities. Mechanism to feed the fuel to the AGNs probably having the super-massive black-holes (SMBHs), in the DHC of a 20 cMpc scale, should be intensively studied and revealed.

In the three-dimensional LBG distribution of Bielby et al. (2011), a small fraction of AGNs seems to exist in LBG LDRs or voids. It usually means that their AGNs are isolated in space, i.e., field objects. However, they may exhibit some correlations with dense H I gas, as discussed above for the SSA22 field. Surveys for them are important and interesting to understand mechanisms of formation and activity of AGNs.

Comparing the present result in this subsection with the work by Cucciati et al. (2014) is interesting. They found a very deep H I absorption dip of a rest-frame EW of -10.8 \AA with the comoving volume of $13 \times 15 \times 17 \text{ cMpc}^3$ at $z = 2.895$ in the COSMOS field through the VIMOS Ultra-Deep Survey (VUDS). Its size is similar to that of our DHC, about $20 \times 20 \times 40 \text{ cMpc}^3$. Also, its rest-frame EW is comparable with our -5 \AA . The great disparity is the counterpart. The absorption dip from Cucciati et al. (2014) is associated with

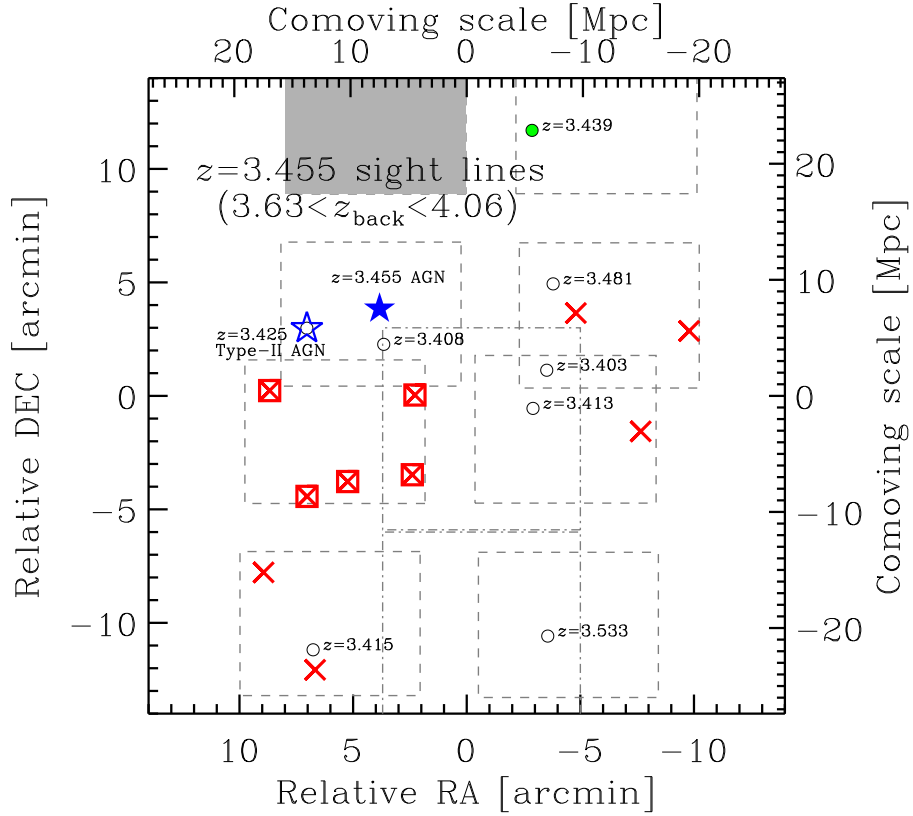


Figure 16. Sky distribution of 10 sight-lines (cross marks) in the plane at $z = 3.455$. The 5 sight-lines showing H I absorption enhancement are indicated by the square enclosing crosses. The Type-I (Type-II) AGN at $z = 3.455$ (3.425) is shown by the filled (open) blue star. The circles indicate the positions of LBGs at $3.40 < z < 3.60$ with their redshifts and one green filled circle is an LBG in the redshift range of the H I absorption enhancement. The gray lines and shaded area are the same as in Figure 6.

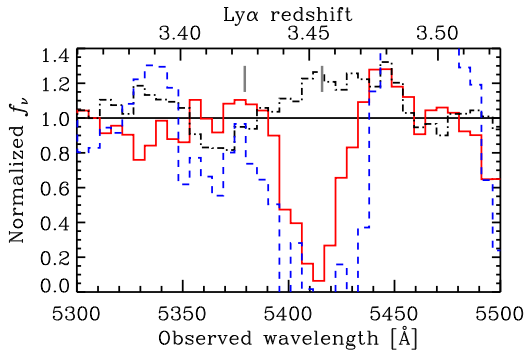


Figure 17. Observer's frame composite spectrum of the LBGs behind of the pair AGN at $z = 3.455$. The solid histogram shows the median composite of the 5 background LBGs south of the pair AGN (those indicated by the square enclosing crosses in Figure 16). The composite spectrum of the other 5 background LBGs in Figure 16 is shown by the dot-dashed histogram. The dashed histogram shows the normalized DA spectrum of the nearest sight-line to the Type-II AGN. The two vertical gray ticks show the redshifts of the AGNs.

a large LBG overdensity of $\delta_{LBG} \sim 12$. However, our deep H I absorption dip does not show such an overdensity peak of LBGs as a counterpart in the present statistics.

We stress that the number density of LBGs is very

large compared to AGNs, i.e., the comoving density of the LBGs with $R < 25.4$ is about 60 times larger than that of the AGNs with $R < 25.4$ from their LFs at $z \sim 3.5$ (Masters et al. 2012). In spite of such popular objects, any LBGs with $R < 25.4$ are not yet detected in the DHC which was found triggered by the presence of the pair of AGNs. As discussed in this paper, the DHCs, the regions showing strong H I absorption dips in the composite spectrum, have a tendency to show significant correlations with LBG overdensities, as the LSPC at $z = 3.1$ for the H I absorption dip at the same redshift and the overdensity of LBGs at $z = 3.26 - 3.31$ discussed in subsection 4.2.4 for the H I dip at $z = 3.28$ in the SSA22 field, together with the LBG sharp peak found at $z = 2.895$ in the COSMOS field described above.

In contrast to those DHCs with LBG HDRs, the DHC we found at $z = 3.453$ has no counterpart LBG overdensity in the present statistics, as mentioned above. It would be exceptional and may suggest peculiar characteristics of this cluster, i.e., the DHC of a 20 cMpc scale discovered at $z = 3.453$ may possess some mechanisms or an extraordinary structure to preferentially generate AGNs but restrict the LBG formation.

Here, it is noteworthy that in the composite spectrum of the 5 sight-lines in the south of the pair AGN, we could not find any significant absorption by C II (1334.53 \AA) as well as Si IV (1393.76 and 1402.77 \AA) associated with the $z = 3.453$ DHC, although the spectral resolution of $R = 180$

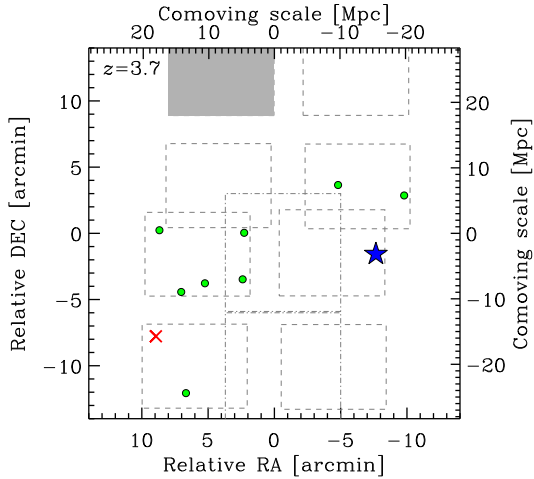


Figure 18. Sky distribution of 8 LBGs (green dots) at $z = 3.69$ – 3.80 which form a bump in redshift distribution shown in Figure 2 (a). The red cross indicates the sky position of the sight-line of the LBG at $z = 4.03$, which is the most distant object in the present survey. The blue star shows the AGN at $z = 3.801$. The gray lines and shaded area are the same as in Figure 6.

is not high enough to put stringent limit on metal enrichment. On the other hand, Cucciati et al. (2014) reported a significant detection of Si IV absorption associated with their DHC having a sharp LBG peak at $z = 2.895$ in their VIMOS survey with a similar spectral resolution of $R = 230$ as ours. Unfortunately, other metal absorption such as Si II (1260.42 Å), O I (1302.17 Å), and Si II (1304.37 Å) associated with the DHC at $z = 3.453$ can not be investigated in our spectroscopic analysis with the low spectral resolution of $R = 180$, because these wavelengths fall in rather wide masked ranges affected by night emission lines indicated by the grey shades in Figure 12 and so on.

It would be very interesting to clarify whether the $z = 3.453$ DHC has less metals or not. Deep spectroscopic survey for LBGs and dense H I gas as well as metals with higher spectral resolution than the present study is strongly desired to confirm the underdensity of LBGs in this region and to investigate the metal abundance of the DHC. If the metal-poor or even metal-free nature in the DHC has been proved in such a survey, the H I cluster will be recognized as a candidate for primordial space survived at $z \sim 3.5$ (e.g., Fumagalli, O’Meara & Prochaska 2011).

6.4 LBG concentration at $z = 3.69$ – 3.80 associated with an AGN and H I absorbers

We can see an LBG bump consisting of 8 LBGs at $z = 3.69$ – 3.80 in the redshift distribution of Figure 2 (a). We show their sky map in Figure 18, where the AGN detected at $z = 3.801$ in VI06 is also plotted with the blue star symbol and a sight-line of the LBG found in VI08 at $z = 4.03$ is indicated by the red cross symbol. Seven out of the 8 LBGs seem to be localized in a belt-like/filamentary structure which extends from west to east with a mean width of about 8 arcmin (16 cMpc) and a length of about 20 arcmin (40 cMpc). We call the filamentary area a candidate HDR.

Although the statistics is insufficient, we try to discuss

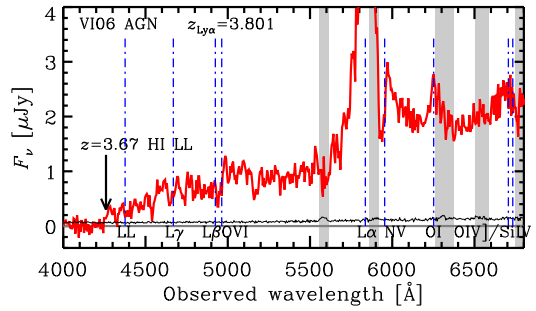


Figure 19. One-dimensional spectrum of the AGN at $z = 3.801$. The LLS is seen at 4255 Å ($z = 3.67$). The gray shaded regions indicate noisy wavelengths due to night emission lines. The vertical dot-dashed lines indicate some emission/absorption features.

the overdensity and appearance probability of this HDR. The thickness of this candidate HDR is estimated to be about 85 cMpc from the redshift interval of the 7 LBGs, $dz = 3.69 - 3.80 = 0.11$. Thus, the comoving volume of the candidate HDR is 5.5×10^4 cMpc³. When LBGs distribute uniformly in this volume, we obtain the expected number of 2.4, assuming the selection function of the dashed line in Figure 5 (a). Therefore, the HDR has a number overdensity $\delta_{\text{LBG}} = 1.9 \pm 1.1$, which results in a mass overdensity $\delta_M = 0.73 \pm 0.42$, when the bias parameter $b = 2.6$ (Bielby et al. 2013; Cucciati et al. 2014) is assumed for the LBGs. The 1σ fluctuation of the dark matter for this volume at $z = 3.75$ is estimated to be 0.13, by using the formula in Yamada et al. (2012a). Thus, the candidate HDR at $z = 3.7$ – 3.8 is also a rare event with $6 \pm 3\sigma$.

It is interesting that the AGN with $z = 3.801$ found in VI06 exists in the envelope region of the candidate HDR as shown in Figure 18. We show the spectrum of the AGN with $R = 22$ AB in Figure 19. Interestingly, we can find a probable LLS at $z = 3.67$, because of a continuum trough at wavelengths shorter than 4255 Å. The following interpretation will be possible, i.e., the candidate HDR has dense H I gas also in its envelope region and the sight-line of the AGN penetrates the H I rich region having the column density of about 10^{18} cm⁻² to make an LLS.

Unlike the cases of the LSPC at $z = 3.1$ and the DHC at $z = 3.453$ associated with the pair AGN, there is only one LBG behind the candidate HDR at $z = 3.75$. Therefore, the composite method in this paper is not practical to investigate H I absorption of the LBG HDR. However, fortunately, a sight-line of the bright LBG of $R = 24.57$ AB at $z = 4.03$ found in the present survey, penetrates the envelope region of the candidate HDR as seen in Figure 18. We show the spectrum of the LBG in Figure 20, which has two remarkable deep absorption dips at $z = 3.69$ and 3.81 , if Ly α absorption is assumed. Their rest-frame equivalent widths are -6 Å and -8 Å respectively, indicating clusters of high column density H I clouds like sub-DLA/LLS.

Although the candidate HDR at $z = 3.75$ includes only 7 LBGs, it has a $z = 3.801$ AGN with a $z = 3.67$ LLS and two deep H I absorption dips at the HDR redshifts in the spectrum of a background LBG, in its surrounding area. We can expect the reality of the structure. Future surveys will reveal the interesting characteristics of this HDR.

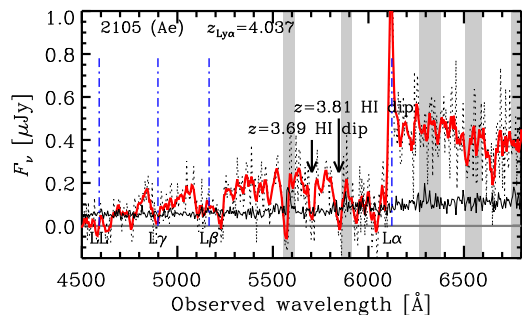


Figure 20. One-dimensional spectrum of the LBG with the highest redshift $z = 4.03$ in this survey. The gray shaded regions indicate noisy wavelengths due to night emission lines. The vertical dot-dashed lines indicate some emission/absorption features.

7 SUMMARY AND CONCLUDING REMARKS

The SSA22 field has a large-scale structure of the LAEs with a comoving volume of around 10^5 Mpc^3 at $z = 3.1$. The structure contains, besides 259 confident LAEs, 35 LABs including two gigantic ones discovered by Steidel et al. (2000), which would be progenitors of the present massive galaxies, as well as hundreds of LBGs, about 50 LAAs, and a number of K-band selected galaxies. So, the structure should be called the “large-scale proto-cluster (LSPC)”. For the field we carried out a spectroscopic survey for LBGs with the VLT VIMOS, VI08 survey, and identified 78 LBGs brighter than $R = 25.4$ AB magnitude with secure spectroscopic redshifts between $z = 2.5$ and 4, and we have obtained the redshift distribution of 171 LBGs, by combining ours with those of Steidel et al. (2003). Also, we stacked the spectra of our VI08 LBGs in the observer’s frame by using the sophisticated method developed in this paper, and obtained the normalized composite spectrum. Analyzing these data, we have obtained the following results;

(1) A strong H I absorption dip of rest-frame equivalent width of -1.7 \AA in the composite transmission spectrum has been found at the LSPC redshift, $z = 3.1$. We have also found an absorption dip at $z = 3.28$ with a sufficient significance. There seems a candidate LBG high density region (HDR) at the same redshift. The combination of LBG concentration and deep H I dip is similar to the $z = 3.1$ structure.

(2) We have detected a remarkable transparency peak at $z = 2.98$ in the composite spectrum, at which an LBG void is found. On the other hand, we have no such peaks at $z = 2.80$ and 2.89 , where there are few LBGs, indicating voids or low-density regions (LDRs) of LBGs. In general, several voids/LDRs would be also expected at redshifts between $z = 2.55$ and 2.8 , where the LBG detection efficiency of our survey decreases. However, no transparency peaks are found at all at those redshifts in spite of the considerable VLT/VIMOS sensitivities for the Ly α forest. It would mean that absence of or less LBGs in the ordinary void itself can not cause such a prominent transparency peak found at $z = 2.98$. The large mass of the 100 cMpc away LSPC at $z = 3.10$ would contribute to the transparency peak formation by the “tidal force”. Such speculative and qualitative considerations are given in Discussion I in section 5.

In the present LBG survey, VI08, we detected four AGNs with $R < 24.6$ and Steidel et al. (2003) also found two AGNs in this field. In addition, we identified five AGNs in our VIMOS survey carried out in 2006, VI06. These 11 AGNs listed in Table 7 distribute in the redshift range of $2.4 < z < 3.8$. In Discussion II in section 6, we have also investigated inhomogeneous structures in large scales accompanied with the AGNs at redshifts between 3.1 and 3.8, and the following interesting results were obtained.

(3) The LSPC at $z = 3.1$ in SSA22 shows an extremely high concentration of AGNs, i.e., there exist 5 AGNs with $R < 24.5$ at redshifts between $z = 3.084$ - 3.132 , where only 0.5 AGNs are expected from the QSO/AGN LF for $z \sim 3.2$ by Masters et al. (2012). In addition to them, 6 AGNs with $R > 24.5$ are found at the LSPC redshift. These 11 AGNs in total at $z \sim 3.1$ exhibit filamentary structure along the LAE density peak.

(4) We have found two LBG HDRs associated with AGNs at $z = 3.353$ and 3.801 , respectively. The former HDR consists of 19 LBGs and the $z = 3.353$ AGN shows a “sheet-like” structure with the appearance probability of $7 \pm 2\sigma$, indicating a very rare event. The other consists of 7 LBGs at redshifts between 3.69 and 3.801 together with the $z = 3.801$ AGN seems to form filamentary structure. The appearance probability of this LBG HDR is estimated to be $6 \pm 3\sigma$, which also implies a rare event, although the statistics is insufficient. The HDR at $z = 3.75$ including only 7 LBGs, however, has an AGN with a $z = 3.67$ LLS of the column density of about 10^{18} cm^{-2} , and two deep H I absorption dips at the HDR redshifts in the spectrum of a background LBG, in its surrounding area. We can expect the reality of the structure.

(5) Near the pair AGN at $z = 3.455$, we found out a 20 cMpc scale dense H I cluster (DHC) by detecting a deep dip at 5415 \AA corresponding to $z = 3.453$, if Ly α absorption is assumed, in the composite spectrum of 5 background LBGs with the angular distances less than 10 arcmin from the center of the pair AGN. Also the spectrum of the AGN at $z = 3.455$ seems to have an LLS at 4050 \AA , i.e., $z = 3.44$, and the spectrum of the nearest sight-line from the partner AGN at $z = 3.425$ shows an absorption feature down to $z = 3.40$ including the AGN redshift, indicating that the DHC includes the pair AGN. Nevertheless, not only the DHC does not associate with any LBG HDR but also there is no LBG around it, in the present statistics, implying a possible underdensity of the LBGs there. If the presence of LBG LDR/void is proven by future observations, the DHC will become a strange cluster showing peculiar characteristics, which preferentially generates AGNs but suppresses LBG formation. Such a region should be intensively studied. If the DHC shows less metal absorption or absence of it in a deep spectroscopic survey with high spectral resolution in future, the H I cluster could become a candidate primordial space survived at $z = 3.45$.

As discussed so far, the SSA22 field has been found to possess a lot of characteristic structures at several successive redshifts, $z = 3.35$, $z = 3.45$ and $z = 3.75$, in addition to the LSPC well established at $z = 3.1$. Each structure has a very rare appearance probability in the present small statistics. If the inhomogeneous structures at $z > 3.3$ are confirmed with better statistics in future spectroscopic surveys, as the

$z = 3.1$ LSPC has already been, the SSA22 field will become one of the key regions to test cosmology beyond the standard Λ CDM model, because the simultaneous appearance of such multiple large- σ events including the LSPC at $z = 3.1$ over a comoving Gpc scale would be unlikely in the standard structure formation scenario based on the gravitational evolution of quantum fluctuation at the inflation epoch.

ACKNOWLEDGMENTS

We thank Jean-Michel Deharveng and Christian Tapken for their contribution to the VIMOS proposal, Ryosuke Yamauchi, Yuki Nakamura, Mitsunori Horie, Eri Nakamura, for discussions and encouragements during the VIMOS data reduction and analysis, Kazuhiro Shimasaku, Masami Ouchi, Ikkoh Shimizu, Olivier Le Fèvre, Eros Vanzella, Joe Hennawi, Monica Turner, Gabor Worseck, and Cameron Hummel for discussions about the results and implications. T.H. is supported by the science research grant of Fujitok Corporation. A.K.I. is supported by JSPS KAKENHI Grant Number 23684010 and 26287034, I.I. is supported by JSPS KAKENHI Grant Number 24244018, and Y.M. is supported by JSPS KAKENHI Grant Number 17H04831 and 17KK0098.

REFERENCES

- Adelberger, K. L., Steidel, C. C., Shapley, A. E., Pettini, M., 2003, *ApJ*, 584, 45
- Adelberger, K. L., Shapley, A. E., Steidel, C. C., Pettini, M., Erb, D. K., Reddy, N. A., 2005, *ApJ*, 629, 636
- Becker, G. D., Hewett, P. C., Worseck, G., Prochaska, J. X., 2013, *MNRAS*, 430, 2067
- Behroozi, P. S., Wechsler, R. H., Conroy, C., 2013, *ApJ*, 770, 57
- Bielby R. M., et al., 2011, *MNRAS*, 414, 2
- Bielby, R., Hill, M. D., Shanks, T., Crighton, N. H. M., Infante, L., Bornancini, C. G., Francke, H., Héraudeau, P., et al., 2013, *MNRAS*, 430, 425
- Boulade, O., Charlot, X., Abbon, P., Aune, S., Borgeaud, P., Carton, P.-H., Carty, M., Da Costa, J., et al., 2003, *SPIE*, 4841, 72
- Bruzual, G., Charlot, S., 2003, *MNRAS*, 344, 1000
- Crighton, N. H. M., Hennawi, J. F., Simcoe, R. A., Cooksey, K. L., Murphy, M. T., Fumagalli, M., Prochaska, J. X., Shanks, T., 2015, *MNRAS*, 446, 18
- Cristiani, S., D’Odorico, S., Fontano, A., Giallongo, E., Savaglio, S., 1995, *MNRAS*, 273, 1016
- Croft, R. A. C., Weinberg, D. H., Pettini, M., Hernquist, L., Katz, N., 1999, *ApJ*, 520, 1
- Cucciati, O., Zamorani, G., Lemaux, B. C., Bardelli, S., Cimatti, A., Le Fèvre, O., Cassata, P., Garilli, B., et al., 2014, *A&A*, 570, 16
- Dekel, A., Birnboim, Y., Engel, G., Freundlich, J., Goerdt, T., Mumcuoglu, M., Neistein, E., Pichon, C., et al., 2009, *Nature*, 457, 451
- Faucher-Giguère, C.-A., Prochaska, J. X., Lidz, A., Hernquist, L., Zaldarriaga, M., 2008, *ApJ*, 681, 831
- Frye, B. L., Bowen, D. V., Hurley, M., Tripp, T. M., Fan, X., Holden, B., Guhathakurta, P., Coe, D., et al., 2008, *ApJ*, 685, L5
- Fumagalli, M., O’Meara, J. M., Prochaska, J. X., 2011, *Science*, 334, 1245
- Gawiser, E., Francke, H., Lai, K., Schawinski, K., Gronwall, C., Ciardullo, R., Quadri, R., Orsi, A., et al., 2007, *ApJ*, 671, 278
- Gehrels N., 1986, *ApJ*, 303, 336
- Giavalisco, M., Vanzella, E., Salimbeni, S., Tripp, T. M., Dickinson, M., Cassata, P., Renzini, A., Guo, Y., et al., 2011, *ApJ*, 743, 95
- Guaita L., et al., 2010, *ApJ*, 714, 255
- Hainline, K. N., Shapley, A. E., Greene, J. E., and Steidel, C. C., 2011, *ApJ*, 733, 31
- Hayashino, T., Matsuda, Y., Tamura, H., Yamauchi, R., Yamada, T., Ajiki, M., Fujita, S. S., Murayama, T., et al., 2004, *AJ*, 128, 2073
- Heckman, T. M., Sembach, K. R., Meurer, G. R., Strickland, D. K., Martin, C. L., Calzetti, D., Leitherer, C., 2001, *ApJ*, 554, 1021
- Hui, L., Rutledge, R. E., 1999, *ApJ*, 517, 541
- Inoue, A. K., Iwata, I., Deharveng, J.-M., Buat, V., Burgarella, D., 2005, *A&A*, 435, 471
- Inoue, A. K., Iwata, I., 2008, *MNRAS*, 387, 1681
- Inoue, A. K., Shimizu, I., Iwata, I., Tanaka, M., 2014, *MNRAS*, 442, 1805
- Kaiser N., 1987, *MNRAS*, 227, 1
- Kirkman, D., Tytler, D., Lubin, D., Charlton, J., 2007, *MNRAS*, 376, 1227
- Komatsu, E., Smith, K. M., Dunkley, J., Bennett, C. L., Gold, B., Hinshaw, G., Jarosik, N., Larson, D., et al., 2011, *ApJS*, 192, 18
- Kousai, K., 2011, Ph.D thesis, Tohoku University
- Lee, K.-G., Hennawi, J. F., White, M., Croft, R. A. C., Ozbek, M., 2014, *ApJ*, 788, 49
- Lee, K.-G., Hennawi, J. F., Stark, C., Prochaska, J. X., White, M., Schlegel, D. J., Eilers, A.-C., Arinyo-i-Prats, A., et al., 2014, *ApJ*, 795, L12
- Lee K.-G., Hennawi, J. F., White, M., Prochaska, J. X., Font-Rivera, A., Schlegel, D. J., Rich, R. M., Suzuki, N., et al., 2016, *ApJ*, 817, 160
- Lee, K.-G., Krolewski, A., White, M., Schlegel, D., Nugent, P. E., Hennawi, J. F., Müller, T., Pan, R., et al., 2018, *ApJS*, 237, 31
- Le Fèvre, O., Saisse, M., Mancini, D., Brau-Nogue, S., Caputi, O., Castinel, L., D’Odorico, S., Garilli, B., et al., 2003, *SPIE*, 4841, 1670
- Lehmer, B. D., Alexander, D. M., Chapman, S. C., Smail, I., Bauer, F. E., Brandt, W. N., Geach, J. E., Matsuda, Y., et al., 2009, *MNRAS*, 400, 299
- Masters D., Capak, P., Salvato, M., Civano, F., Mobasher, B., Siana, B., Hasinger, G., Impey, C. D., et al., 2012, *ApJ*, 755, 169
- Matsuda, Y., Yamada, T., Hayashino, T., Tamura, H., Yamauchi, R., Ajiki, M., Fujita, S. S., Murayama, T., et al., 2004, *AJ*, 128, 569
- Matsuda, Y., Yamada, T., Hayashino, T., Tamura, H., Yamauchi, R., Murayama, T., Nagao, T., Ohta, K., Okamura, S., et al., 2005, *ApJ*, 634, L125
- Matsuda, Y., Yamada, T., Hayashino, T., Yamauchi, R., Nakamura, Y., 2006, *ApJ*, 640, L123
- Matsuda, Y., Richard, J., Smail, I., Kashikawa, N., Shimasaku, K., Frye, B. L., Yamada, T., Nakamura, Y., et al., 2010, *MNRAS*, 403, L54
- Matsuda, Y., Yamada, T., Hayashino, T., Yamauchi, R., Nakamura, Y., Morimoto, N., Ouchi, M., Ono, Y., et al., 2012, *MNRAS*, 425, 878
- Mawatari, K., Yamada, T., Nakamura, Y., Hayashino, T., Matsuda, Y., 2012, *ApJ*, 759, 133
- Mawatari, K., Inoue, A. K., Kousai, K., Hayashino, T., Cooke, R., Prochaska, J. X., Yamada, T., Matsuda, Y., 2016, *ApJ*, 817, 161
- Mawatari K., et al., 2017, *MNRAS*, 467, 3951
- McDonald, P., Miralda-Escudé, J., Rauch, M., Sargent, W. L. W., Barlow, T. A., Cen, R., Ostriker, J. P., 2000, *ApJ*, 543, 1
- Meiksin, A., Bouchet, F. R., 1995, *ApJ*, 448, L85

- Micheva G., Iwata I., Inoue A. K., 2017, *MNRAS*, 465, 302
- Miyazaki, S., Komiyama, Y., Sekiguchi, M., Okamura, S., Doi, M., Furusawa, H., Hamabe, M., Imi, K., et al., 2002, *PASJ*, 54, 833
- Momose, R., Ouchi, M., Nakajima, K., Ono, Y., Shibuya, T., Shimasaku, K., Yuma, S., Mori, M., et al., 2014, *MNRAS*, 442, 110
- Oke, J. B., 1974, *ApJS*, 236, 21
- Press, W. H., Teukolsky, S. A., Vetterling, W. T., Flannery, B. P., 1992, *Numerical Recipes*, Second Edition, Cambridge University Press
- Prochaska, J. X., Hennawi, J. F., Lee, K.-G., Cantalupo, S., Bovy, J., Djorgovski, S. G., Ellison, S. L., Lau, M. W., et al., 2013, *ApJ*, 776, 136
- Prochaska, J. X., Lau, M. W., Hennawi, J. F., 2014, *ApJ*, 796, 140
- Rakic, O., Schaye, J., Steidel, C. C., Rudie, G. C., 2012, *ApJ*, 751, 94
- Rakic, O., Schaye, J., Steidel, C. C., Booth, C. M., Dalla Vecchia, C., Rudie, G. C., 2013, *MNRAS*, 433, 3103
- Reddy, N., Steidel, C. C., 2009, *ApJ*, 692, 778
- Rudie, G. C., Steidel, C. C., Trainor, R. F., Rakic, O., Bogosavljevic, M., Pettini, M., Reddy, N., Shapley, A. E., Erb, D. K., Law, D. R., 2012, *ApJ*, 750, 67
- Saez, C., Lehmer, B. D., Bauer, F. E., Stern, D., Gonzales, A., Rreza, I., Alexander, D. M., Matsuda, Y., et al., 2015, *MNRAS*, 450, 2615
- Sawicki, M., Thompson, D., 2006, *ApJ*, 642, 653
- Sawicki, M., 2012, *MNRAS*, 421, 2187
- Shapley, A. E., Steidel, C. C., Pettini, M., Adelberger, K. L., 2003, *ApJ*, 588, 65
- Springel, V., White, S. D. M., Jenkins, A., Frenk, C. S., Yoshida, N., Gao, L., Navarro, J., Thacker, R., et al., 2005, *Nature*, 435, 629
- Stark, C. W., White, M., Lee, K.-G., Hennawi, J. F., 2015a, *MNRAS*, 453, 311
- Strak, C. W., Font-Rivera, A., White, M., Lee, K.-G., 2015b, *MNRAS*, 453, 4311
- Steidel, C. C., Pettini, M., Hamilton, D., 1995, *AJ*, 110, 2519
- Steidel, C. C., Adelberger, K. L., Dickinson, M., Giavalisco, M., Pettini, M., Kellogg, M., 1998, *ApJ*, 492, 428
- Steidel, C. C., Adelberger, K. L., Giavalisco, M., Dickinson, M., Pettini, M., 1999, *ApJ*, 519, 1
- Steidel, C. C., Adelberger, K. L., Shapley, A. E., Pettini, M., Dickinson, M., Giavalisco, M., 2000, *ApJ*, 532, 170
- Steidel, C. C., Adelberger, K. L., Shapley, A. E., Pettini, M., Dickinson, M., Giavalisco, M., 2003, *ApJ*, 592, 728
- Steidel, C. C., Erb, D. K., Shapley, A. E., Pettini, M., Reddy, N., Bogosavljevic, M., Rudie, G. C., Rakic, O., 2010, *ApJ*, 717, 289
- Steidel, C. C., Bogosavljevic, M., Shapley, A. E., Kollmeier, J. A., Reddy, N. A., Erb, D. K., Pettini, M., 2011, *ApJ*, 736, 160
- Tejos, N., Morris, S. L., Crighton, N. H. M., Theuns, T., Altay, G., Finn, C. W., 2012, *MNRAS*, 425, 245
- Thomas, R., Le Fèvre, O., Cassata, V., Le Brun P., Garilli, B., Lemaux, B. C., Maccagni, D., Pentericci, L., et al., 2015, *A&A*, submitted (arXiv:1411.5692)
- Topping, M. W., Shapley, A. E., Steidel, C. C., 2016, *ApJ*, 824, L11
- Topping, M. W., Shapley, A. E., Steidel, C. C., Naoz, S., Primack, J. R., 2018, *ApJ*, 852, 134
- Turner, M. L., Schaye, J., Steidel, C. C., Rudie, G. C., Strom, A. L., 2014, *MNRAS*, 445, 794
- Uchimoto Y. K., et al., 2012, *ApJ*, 750, 116
- Yamada, T., Nakamura, Y., Matsuda, Y., Hayashino, T., Yamauchi, R., Morimoto, N., Kousai, K., Umemura, M., 2012, *AJ*, 143, 79
- Yamada, T., Matsuda, Y., Kousai, K., Hayashino, T., Morimoto, N., Umemura, M., 2012, *ApJ*, 751, 29
- Yoshida, M., Shimasaku, K., Ouchi, M., Sekiguchi, K., Furusawa, H., Okamura, S., 2008, *ApJ*, 679, 269
- Zuo, L., Bond, J. R., 1994, *ApJ*, 423, 73

APPENDIX A: REDSHIFT CATALOG OF LBGs IN THE SSA22 FIELD

Table A.1 is the catalog of LBGs whose redshifts are determined by our VLT/VIMOS observations. If u^* magnitudes are fainter than $1-\sigma$ magnitude (27.8 AB), we list the value as upper limits of brightness. These tables are published only in the on-line version.

Table A1. Redshift catalog of LBGs in VIMOS 2008 observations.

Slit	ID	RA (J2000)	DEC (J2000)	z_{sys}	Category	u^* [AB]	B [AB]	V [AB]	R_c [AB]	i' [AB]	z' [AB]
1102	116487	22:18:05.97	0:23:14.67	2.921	Ae	26.13	25.29	24.78	24.75	24.61	24.73
1109	104357	22:17:42.58	0:20:54.73	3.168	Ae	26.16	24.90	23.98	24.13	24.01	24.03
1111	100623	22:17:37.14	0:20:04.63	2.732	Ae	26.47	25.76	25.11	25.19	24.96	24.87
1114	99220	22:18:04.14	0:19:46.88	3.418	Ae	27.50	26.21	24.91	24.62	24.36	24.48
1117	96352	22:18:04.33	0:19:17.08	3.013	Ae	26.85	25.67	25.13	25.05	24.98	25.08
...											